Mon. Not. R. Astron. Soc. **000**, 000–000 (0000) Printed November 11, 2014 (MN LATEX style file v2.2)

Visibility based angular power spectrum estimation in low frequency radio interferometric observations

Samir Choudhuri[1⋆], Somnath Bharadwaj[1]†, Abhik Ghosh[2] and SK. Saiyad Ali[3]
[1] *Department of Physics, & Centre for Theoretical Studies, IIT Kharagpur, Pin: 721 302, India*
[2] *Kapteyn Astronomical Institute, PO Box 800, 9700 AV Groningen, The Netherlands*
[3] *Department of Physics,Jadavpur University, Kolkata 700032, India*

arXiv:1409.7789v2 [astro-ph.CO] 10 Nov 2014

ABSTRACT

We present two estimators to quantify the angular power spectrum of the sky signal directly from the visibilities measured in radio interferometric observations. This is relevant for both the foregrounds and the cosmological 21-cm signal buried therein. The discussion here is restricted to the Galactic synchrotron radiation, the most dominant foreground component after point source removal. Our theoretical analysis is validated using simulations at 150 MHz, mainly for GMRT and also briefly for LOFAR. The Bare Estimator uses pairwise correlations of the measured visibilities, while the Tapered Gridded Estimator uses the visibilities after gridding in the uv plane. The former is very precise, but computationally expensive for large data. The latter has a lower precision, but takes less computation time which is proportional to the data volume. The latter also allows tapering of the sky response leading to sidelobe suppression, an useful ingredient for foreground removal. Both estimators avoid the positive bias that arises due to the system noise. We consider amplitude and phase errors of the gain, and the w-term as possible sources of errors . We find that the estimated angular power spectrum is exponentially sensitive to the variance of the phase errors but insensitive to amplitude errors. The statistical uncertainties of the estimators are affected by both amplitude and phase errors. The w-term does not have a significant effect at the angular scales of our interest. We propose the Tapered Gridded Estimator as an effective tool to observationally quantify both foregrounds and the cosmological 21-cm signal.

Key words: methods: statistical, data analysis - techniques: interferometric- cosmology: diffuse radiation

1 INTRODUCTION

Observations of the redshifted 21-cm radiation from the large scale distribution of neutral hydrogen (HI) is one of the most promising probes to study the high redshift Universe (recent reviews: Morales & Wyithe 2010; Mellema et al. 2013). This radiation appears as a very faint, diffuse background radiation in all low frequency radio observations below 1420 MHz. At these frequencies the sky signal is largely dominated by different foregrounds which are four to five orders of magnitude stronger than the redshifted 21 cm signal (Ali, Bharadwaj & Chengalur 2008; Bernardi et al. 2009; Ghosh et al. 2012; Pober et al. 2013). Foreground removal is possibly the most serious challenge for detecting the cosmological 21-cm signal. Various methodologies have been explored for foreground subtraction and for detecting the underlying 21 cm signal (Bowman, Morales & Hewitt 2009; Jelic et al. 2010; Ghosh et al. 2011b; Paciga et al. 2011; Petrovic & Oh 2011; Vedantham et al. 2012; Mao 2012; Liu & Tegmark 2012; Cho et al. 2012; Trott et al. 2012; Chapman et al. 2012, 2013; Thyagarajan et al. 2013; Paciga et al. 2013; Jacobs et al. 2013; Parsons et al. 2014; Dillon et al. 2014; Shaw et al. 2014a; Liu et al. 2014a,b).

The Galactic synchrotron emission is expected to be the most dominant foreground at angular scale $> 10^{'}$ after point source subtraction at $10 - 20$ mJy level (Bernardi et al. 2009; Ghosh et al. 2012). A precise characterization and a detailed

⋆ Email:samir11@phy.iitkgp.ernet.in
† Email:somnath@phy.iitkgp.ernet.in

understanding of the Galactic synchrotron emission is needed to reliably remove foregrounds in 21 cm experiments. The study of the Galactic synchrotron emission is interesting in its own right. This will shed light on the cosmic ray electron distribution, the strength and structure of the Galactic magnetic field, and the magnetic turbulence (Waelkens et al. 2009; Lazarian & Pogosyan 2012; Iacobelli et al. 2013).

Bernardi et al. (2009) and Ghosh et al. (2012) have respectively analyzed 150 MHz WSRT and GMRT observations where they find that the measured angular power spectrum can be well fitted with a power law ($C_\ell \propto \ell^{-\beta}$, $\beta = 2.2 \pm 0.3$ for WSRT and $\beta = 2.34 \pm 0.28$ for GMRT) upto $\ell \leq 900$. At relatively higher frequencies, Giardino et al. (2001) and Giardino et al. (2002) have analyzed the fluctuations in the Galactic synchrotron radiation using the 2.3 GHz Rhodes Survey and the 2.4 GHz Parkes radio continuum and polarization survey, where they find a slope $\beta = 2.43 \pm 0.01$ ($2 \leq \ell \leq 100$) and $\beta = 2.37 \pm 0.21$ ($40 \leq \ell \leq 250$) respectively. At tens of GHz, Bennett et al. (2003) have determined the angular power spectrum of the Galactic synchrotron radiation using the Wilkinson Microwave Anisotropy Probe (WMAP) data where they find a scaling $C_\ell \sim \ell^{-2}$ within $\ell \leq 200$. The structure of the Galactic synchrotron emission is not well quantified at the frequencies and angular scales relevant for detecting the cosmological 21-cm signal, and there is considerable scope for further work in this direction.

Radio interferometric observations measure the complex visibility. The measurement is done directly in Fourier space which makes interferometers ideal instruments for measuring the angular power spectrum of the sky signal. The visibility based power spectrum estimator formalism has been extensively used for analyzing CMB data from interferometers (Hobson et al. 1995; White et al. 1999; Hobson et al. 2002; Myers et al. 2003). A visibility based estimator has also been successfully employed to study the power spectrum of the HI in the interstellar medium (ISM) of several nearby galaxies (e.g. Begum et al. 2006; Dutta et al. 2009). A direct visibility based approach has been proposed for quantifying the power spectrum of the cosmological 21-cm signal expected at the GMRT (Bharadwaj & Sethi 2001; Bharadwaj & Pandey 2003; Bharadwaj & Ali 2005) and recently for the ORT (Ali & Bharadwaj 2013). Visibility based power spectrum estimators have been used to analyze GMRT data in the context of HI observations (Ali, Bharadwaj & Chengalur 2008; Paciga et al. 2011; Ghosh et al. 2011a,b, 2012). A recent paper (Paul et al. 2014) has proposed visibility correlations to detect the EoR signal using drift scan observations with the MWA .

It is possible to estimate the angular power spectrum of the sky signal from the synthesized radio image (e.g. Bernardi et al. 2009, 2010; Iacobelli et al. 2013). The noise properties of the visibilities are better understood than those of the image pixels. The noise in the different visibilities is uncorrelated, whereas the noise in the image pixels may be correlated depending on the baseline uv coverage. The visibility based power spectrum estimators have the added advantage that they avoid possible imaging artifacts due to the dirty beam, etc (Trott et al. 2011).

In this paper we consider two estimators which use the measured visibilities to quantify the angular power spectrum of the sky signal. The Bare Estimator, which has been utilized in Ali, Bharadwaj & Chengalur (2008) and Ghosh et al. (2011a), directly uses pairwise correlations of the measured visibilities. The Tapered Gridded Estimator, which has been utilized in Ghosh et al. (2011b) and Ghosh et al. (2012), uses the visibilities after gridding on a rectangular grid in the uv plane. The latter incorporates the feature that it allows a tapering of the sky response and thereby suppresses the sidelobes of the telescope's primary beam. Earlier work (Ghosh et al. 2011b) has shown this to be a useful ingredient in foreground removal for detecting the cosmological 21-cm signal. In this paper we have carried out a somewhat detailed investigation in order to place these two estimators on sound theoretical footing. The theoretical predictions are substantiated using simulations. As a test-bed for the estimators, we consider a situation where the point sources have been identified and subtracted out so that the residual visibilities are dominated by the Galactic synchrotron radiation. We investigate how well the estimators are able to recover the angular power spectrum of the input model used to simulate the Galactic synchrotron emission at 150 MHz. We have also analyzed the effects of gain errors and the w-term. Most of our simulations are for the GMRT, but we also briefly consider simulations for LOFAR. The estimators considered here can be generalized to the multi-frequency angular power spectrum (MAPS, Datta, Roy Choudhury & Bharadwaj 2007) which can be used to quantify the cosmological 21-cm signal. We plan to investigate this in a future study.

A brief outline of the paper follows. In Section 2 we establish the relation between the visibility correlation and the angular power spectrum. In Section 3 we describe the simulations which we have used to validate the theoretical results of this paper. In Sections 4 and 5 we consider the Bare and the Tapered Gridded Estimators respectively. The theoretical analysis and the results from the simulations are all presented in these two sections. Section 6 presents a brief comparison between the two estimators, and in Sections 7 and 8 we consider the effect of gain errors and the w-term respectively. Much of the analysis of the previous sections is in the context of the GMRT. In Section 9 we apply the estimators to simulated LOFAR data and present the results. We present discussion and conclusions in Section 10.

2 VISIBILITY CORRELATIONS AND THE ANGULAR POWER SPECTRUM

In this section we discuss the relation between the two visibility correlation and the angular power spectrum of the specific intensity $I(\vec{\theta}, \nu)$ or equivalently the brightness temperature $T(\vec{\theta}, \nu)$ distribution on the sky under the flat-sky approximation.

Here $\vec{\theta}$ is a two dimensional vector on the plane of the sky with origin at the center of the field of view (FoV). It is useful to decompose the specific intensity as $I(\vec{\theta},\nu) = \bar{I}(\nu)+\delta I(\vec{\theta},\,\nu)$ where the first term $\bar{I}(\nu)$ is an uniform background brightness and the second term $\delta I(\vec{\theta},\,\nu)$ is the angular fluctuation in the specific intensity. We assume that $\delta I(\vec{\theta},\,\nu)$ is a particular realization of a statistically homogeneous and isotropic Gaussian random process on the sky. In radio interferometric observations, the fundamental observable quantity is a set of complex visibilities $\mathcal{V}(\mathbf{U},\nu)$ which are sensitive to only the angular fluctuations in the sky signal. The baseline $\mathbf{U}$ quantifies the antenna pair separation $\mathbf{d}$ projected on the plane perpendicular to the line of sight in units of the observing wavelength λ. The measured visibilities are a sum of two contributions $\mathcal{V}(\mathbf{U},\nu) = \mathcal{S}(\mathbf{U},\nu)+\mathcal{N}(\mathbf{U},\nu)$, the sky signal and system noise respectively. We assume that the signal and the noise are both uncorrelated Gaussian random variables with zero mean. The visibility contribution $\mathcal{S}(\mathbf{U},\nu)$ from the sky signal records the Fourier transform of the product of the primary beam pattern $\mathcal{A}(\vec{\theta},\nu)$ and $\delta I(\vec{\theta},\,\nu)$. The primary beam pattern $\mathcal{A}(\vec{\theta},\nu)$ quantifies how the individual antenna responds to signals from different directions in the sky. Using the convolution theorem, we then have

$$\mathcal{S}(\mathbf{U},\nu) = \int d^2U'\,\tilde{a}\left(\mathbf{U}-\mathbf{U}',\,\nu\right)\;\Delta\tilde{I}(\mathbf{U}',\,\nu), \tag{1}$$

where $\Delta\tilde{I}(\mathbf{U},\,\nu)$ and $\tilde{a}\,(\mathbf{U},\nu)$ are the Fourier transforms of $\delta I(\vec{\theta},\,\nu)$ and $\mathcal{A}(\vec{\theta},\,\nu)$ respectively. Typically, the term arising from the uniform specific intensity distribution $\bar{I}(\nu)\tilde{a}\,(\mathbf{U},\nu)$ makes no contribution to the measured visibilities, and we have dropped this. We refer to $\tilde{a}\,(\mathbf{U},\nu)$ as the aperture power pattern. The individual antenna response $\mathcal{A}(\vec{\theta},\nu)$ for any telescope is usually quite complicated depending on the telescope aperture, the reflector and the feed (Christiansen & Hogbom 1969). It is beyond the scope of the present paper to consider the actual single antenna response of any particular telescope. We make the simplifying assumption that the telescope has an uniformly illuminated circular aperture of diameter D whereby we have the primary beam pattern (Figure 1)

$$\mathcal{A}(\vec{\theta},\,\nu) = \left[\left(\frac{2\lambda}{\pi\theta D}\right) J_1\left(\frac{\pi\theta D}{\lambda}\right)\right]^2 \tag{2}$$

where J_1 is the Bessel function of the first kind of order one, the primary beam pattern is normalized to unity at the pointing center $[\mathcal{A}(0) = 1]$, and the aperture power pattern is

$$\tilde{a}(\mathbf{U},\nu) = \frac{8\lambda^4}{\pi^2 D^4}\left[\left(\frac{D}{\lambda}\right)^2 \cos^{-1}\left(\frac{\lambda U}{D}\right) - U\sqrt{\left(\frac{D}{\lambda}\right)^2 - U^2}\right], \tag{3}$$

We note that $\tilde{a}(\mathbf{U},\nu)$ in eq. (3) peaks at $U = 0$, declines monotonically with increasing U, and is zero for $U \geq D/\lambda$. The primary beam pattern (Figure 1) is well approximated by a circular Gaussian function

$$\mathcal{A}_G(\vec{\theta},\nu) = \exp[-\theta^2/\theta_0^2] \tag{4}$$

of the same full width at half maxima (FWHM) as eq. (2). The parameter θ_0 here is related to the full width half maxima $\theta_{\rm FWHM}$ of the primary beam pattern $\mathcal{A}(\vec{\theta},\nu)$ (eq. 2) as $\theta_0 = 0.6\theta_{\rm FWHM}$, and

$$\tilde{a}_G(\mathbf{U},\nu) = \frac{1}{\pi U_0^2}\; e^{-U^2/U_0^2} \tag{5}$$

where $U_0 = (\pi\theta_0)^{-1} = 0.53/\theta_{\rm FWHM}$. While the Gaussian $\tilde{a}_G(\mathbf{U},\nu)$ (eq. 5) provides a good approximation to $\tilde{a}(\mathbf{U},\nu)$ (eq. 3) particularly in the vicinity of $U = 0$, there is however a significant difference in that $\tilde{a}(\mathbf{U},\nu)$ has a compact support and is exactly zero for all $U \geq D/\lambda$ whereas $\tilde{a}_G(\mathbf{U},\nu)$, though it has an extremely small value for $U \geq D/\lambda$, does not become zero anywhere. In practice it is extremely difficult to experimentally determine the full primary beam pattern $\mathcal{A}(\vec{\theta},\,\nu)$ for a telescope. However, the value of $\theta_{\rm FWHM}$ is typically well determined. This has motivated the Gaussian approximation to be used extensively for both theoretical predictions (Bharadwaj & Sethi 2001; Bharadwaj & Ali 2005) and analyzing observational data (Ali, Bharadwaj & Chengalur 2008; Ghosh et al. 2012). The close match between $\mathcal{A}(\vec{\theta},\,\nu)$ (eq. 2) and $\mathcal{A}_G(\vec{\theta},\,\nu)$ (eq. 4) indicates that we may also expect the Gaussian approximation to provide a good fit to the telescope's actual primary beam pattern, particularly within the main lobe. This, to some extent, justifies the use of the Gaussian approximation in the earlier works. The Gaussian approximation simplifies the calculations rendering them amenable to analytic treatment, and we use it on several occasions as indicated later in this paper. For much of the investigations presented in this paper we have considered $D = 45$ m and $\lambda = 2$ m which corresponds to GMRT 150 MHz observations. We have also considered $D = 30.75$ m and $\lambda = 2$ m which corresponds to LOFAR 150 MHz observations. For both these telescopes, Table 1 summarizes the values of some of the relevant parameters. Note that these values correspond to the idealized telescope model discussed above, and they are somewhat different from the values actually measured for the respective telescopes. For example, the GMRT primary beam pattern has $\theta_{\rm FWHM} = 186^{'}$ whereas we have used $\theta_{\rm FWHM} = 157^{'}$ based on our idealized model. We discuss the observational consequence of this $\sim 16\%$ difference later in Section 10 of this paper. For the rest of this paper we focus on the GMRT , except in Section 9 where we shift our attention to LOFAR. Our entire analysis is based on the idealized telescope model described above and the relevant parameters are listed in Table 1 for both these telescopes.

In the flat sky approximation the statistical properties of the background intensity fluctuations $\delta I(\vec{\theta},\,\nu)$ can be quantified

150 MHz	D	$\theta_{\rm FWHM}$	θ_0	U_0	σ_0
		$1.03\lambda/D$	$0.6\theta_{\rm FWHM}$	$0.53/\theta_{\rm FWHM}$	$0.76/\theta_{\rm FWHM}$
GMRT	45 m	$157^{'}$	$95^{'}$	11.54	16.6
LOFAR	30.75 m	$230^{'}$	$139^{'}$	7.88	11.33

Table 1. This shows some relevant parameters for the primary beam pattern calculated using the idealized telescope model (eqs. 2,3), and the Gaussian approximation (eqs. 4,5). The parameter σ_0 is defined in eq. (10).

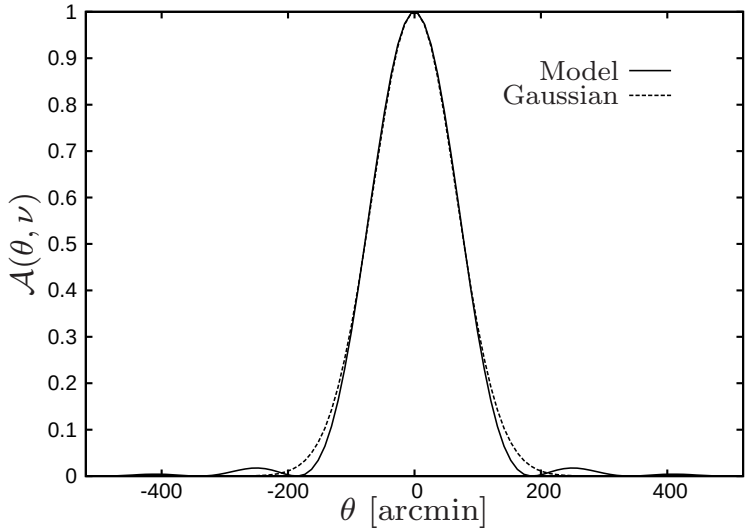

Figure 1. The solid curve shows the 150 MHz GMRT primary beam pattern $\mathcal{A}(\vec{\theta},\,\nu)$ predicted by eq. (2), and the dashed curve shows Gaussian approximation (eq. 4) with the same $\theta_{\rm FWHM}$.

through the two dimensional (2D) power spectrum $P(U,\nu)$ defined as,

$$\langle \Delta\tilde{I}(\mathbf{U},\nu)\Delta\tilde{I}^{*}(\mathbf{U}',\nu)\rangle = \delta_D^2(\mathbf{U}-\mathbf{U}')\,P(U,\nu), \tag{6}$$

where $\delta_D^2(\mathbf{U}-\mathbf{U}')$ is a two dimensional Dirac delta function. The angular brackets $\langle ...\rangle$ here denote an ensemble average over different realizations of the stochastic intensity fluctuations on the sky. We also assume that the $P(U,\nu)$ depends only on the magnitude $U=|\mathbf{U}|$ *i.e.* the fluctuations are statistically isotropic. We note that $P(U,\nu)$ is related to $C_\ell(\nu)$ the angular power spectrum of the brightness temperature fluctuations through (Ali, Bharadwaj & Chengalur 2008)

$$C_\ell(\nu) = \left(\frac{\partial B}{\partial T}\right)^{-2} P(\ell/2\pi,\nu)\,, \tag{7}$$

where the angular multipole ℓ corresponds to $U=\ell/2\pi$, B is the Planck function and $(\partial B/\partial T)=2k_B/\lambda^2$ in the Raleigh-Jeans limit which is valid at the frequencies of our interest. We will drop the ν dependence henceforth as the rest of the calculations are done at a fixed frequency $\nu=150\,$MHz.

We now consider the two visibility correlation which is defined as

$$V_2(\mathbf{U},\mathbf{U}+\Delta\mathbf{U}) = \langle \mathcal{V}(\mathbf{U})\mathcal{V}^{*}(\mathbf{U}+\Delta\mathbf{U})\rangle\,, \tag{8}$$

and which has the contribution

$$S_2(\mathbf{U},\mathbf{U}+\Delta\mathbf{U}) = \int d^2U'\,\tilde{a}(\mathbf{U}-\mathbf{U}')\,\tilde{a}^{*}(\mathbf{U}+\Delta\mathbf{U}-\mathbf{U}')\,P(U') \tag{9}$$

from the sky signal.

The visibilities at the baselines $\mathbf{U}$ and $\mathbf{U}+\Delta\mathbf{U}$ are correlated only if there is a significant overlap between $\tilde{a}(\mathbf{U}-\mathbf{U}')$ and $\tilde{a}^{*}(\mathbf{U}+\Delta\mathbf{U}-\mathbf{U}')$. The correlation $S_2(\mathbf{U},\mathbf{U}+\Delta\mathbf{U})$ is strongest when $|\Delta\mathbf{U}|=0$, declines rapidly with increasing $|\Delta\mathbf{U}|$, and is zero for $|\Delta\mathbf{U}|\geq 2D/\lambda$. The correlation $S_2(\mathbf{U},\mathbf{U}+\Delta\mathbf{U})$ depends on both, the magnitude of $\Delta\mathbf{U}$ as well as the angle between $\Delta\mathbf{U}$ and $\mathbf{U}$, and an earlier work (Bharadwaj & Pandey 2003) has studied this in detail for the predicted post-reionization cosmological 21-cm signal. In this work we have considered a power law power spectrum $P(U)=AU^{-\beta}$ for different values of β in the range 1.5 to 3.5, and we have used eq. (9) to study the $\Delta\mathbf{U}$ dependence of $S_2(\mathbf{U},\mathbf{U}+\Delta\mathbf{U})$. We find that the $\Delta\mathbf{U}$

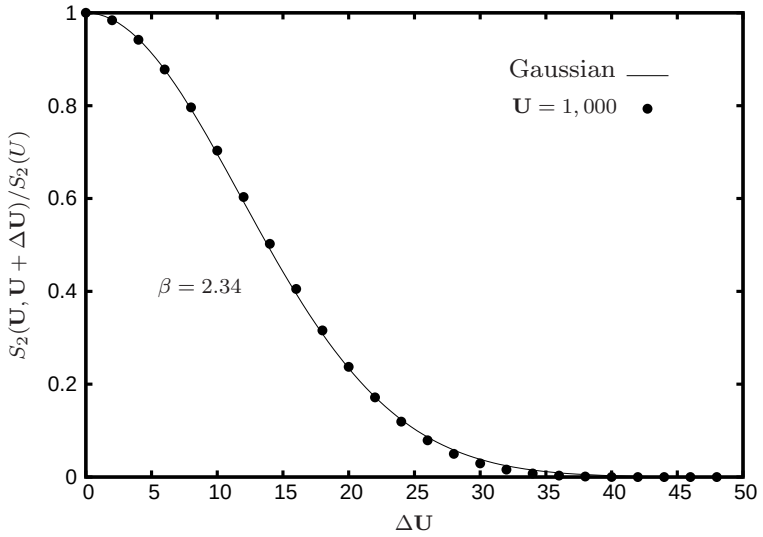

Figure 2. This figure shows how the sky signal contribution to the two visibility correlation varies with $\Delta\mathbf{U}$ for a fixed value $U = 1,000$. The points show the results from eq. (9) for $P(U) = AU^{-2.34}$, and the solid line shows the Gaussian fit given in eq. (10).

dependence is isotropic to a great extent, and it can be well modelled using a Gaussian (Figure 2) as

$$S_2(\mathbf{U}, \mathbf{U} + \Delta\mathbf{U}) = \exp\left[- \left(\frac{\mid \Delta\mathbf{U} \mid}{\sigma_0} \right)^2 \right] S_2(U), \tag{10}$$

where $\sigma_0 = 0.76/\theta_{\rm FWHM}$ (Table 1) and $S_2(U) \equiv S_2(\mathbf{U}, \mathbf{U})$. While the approximation in eq. (10) matches the result of eq. (9) quite well for small $\Delta\mathbf{U}$, the approximation breaks down when $\mid \Delta\mathbf{U} \mid > 2D/\lambda$ where $S_2(\mathbf{U}, \mathbf{U} + \Delta\mathbf{U}) = 0$ contrary to the prediction of eq. (10). This discrepancy, however, does not significantly affect the estimators (defined later) because the value of $S_2(\mathbf{U}, \mathbf{U} + \Delta\mathbf{U})$ predicted by eq. (10) is extremely small for $\mid \Delta\mathbf{U} \mid > 2D/\lambda$.

A further simplification is possible for $U \gg U_0$ where it is possible to approximate $S_2(U)$ which is calculated using eq. (9) by assuming that the value of $P(U')$ does not change much within the width of the function $|\tilde{a}\,(\mathbf{U} - \mathbf{U}')\,|^2$. We then obtain

$$S_2(U) = \left[\int d^2U' \;\mid \tilde{a}(\mathbf{U} - \mathbf{U}')\mid^2 \right] P(U)\,. \tag{11}$$

The integral in the square brackets has a constant value $\frac{\pi\theta_0^2}{2}$ in the Gaussian approximation which yields the value 1.19×10^{-3}, whereas we have 1.15×10^{-3} if we use eq. (3) and numerically evaluate the integral in the square brackets. We see that the Gaussian approximation is adequate for the integral in eq. (11), and we adopt the value $\pi\theta_0^2/2$ for the entire subsequent analysis. We have calculated $S_2(U)$ (Figure.3) using the convolution in eq. (9), and compared this with the approximation in eq. (11). We find that the approximation in eq. (11) matches quite well with the convolution (eq. 9) for baselines $U \geq 4U_0 \sim 45$. Throughout the subsequent analysis we have restricted the baselines to this range, and we have used eq. (11) to evaluate $S_2(U)$, the sky signal contribution to the visibility correlation.

We finally have the approximate relation between the sky signal contribution to the two visibility correlation and the angular power spectrum

$$S_2(\mathbf{U}, \mathbf{U} + \Delta\mathbf{U}) = \frac{\pi\theta_0^2}{2} \left(\frac{\partial B}{\partial T} \right)^2 \exp\left[- \left(\frac{\Delta U}{\sigma_0} \right)^2 \right] C_\ell \tag{12}$$

where $\ell = 2\pi U$. We thus see that the visibilities at two different baselines $\mathbf{U}$ and $\mathbf{U} + \Delta\mathbf{U}$ are correlated only if the separation is small ($\mid \Delta U \mid \leq \sigma_0$), and there is negligible correlation if the separation is beyond a disk of radius σ_0. Further, the visibility correlation $S_2(\mathbf{U}, \mathbf{U} + \Delta\mathbf{U})$ gives a direct estimate of the angular power spectrum C_ℓ at the angular multipole $\ell = 2\pi U$. In addition to the sky signal $\mathcal{S}(\mathbf{U})$, each visibility also contains a system noise contribution $\mathcal{N}(\mathbf{U})$. For each visibility measurement, the real and imaginary parts of $\mathcal{N}(\mathbf{U})$ are both random variables of zero mean and rms. σ_n. Further, the noise in any two different visibilities is uncorrelated. We can then write the total visibility correlation as

$$V_{2ij} \equiv \langle \mathcal{V}_i \mathcal{V}_j^* \rangle = V_0\, e^{-|\Delta\mathbf{U}_{ij}|^2/\sigma_0^2}\, C_{\ell_i} + \delta_{ij} 2\sigma_n^2 \tag{13}$$

where $[\mathcal{V}_i, \mathcal{V}_j] \equiv [\mathcal{V}(\mathbf{U}_i), \mathcal{V}(\mathbf{U}_j)]$, $V_0 = \frac{\pi\theta_0^2}{2} \left(\frac{\partial B}{\partial T}\right)^2$, $\Delta\mathbf{U}_{ij} = \mathbf{U}_i - \mathbf{U}_j$ and the Kronecker delta δ_{ij} is nonzero only if we correlate a visibility with itself. Equation (13) relates the two visibility correlation V_{2ij} to C_{ℓ_i} the angular power spectrum of the sky signal at the angular multipole $\ell_i = 2\pi U_i$ and σ_n^2 the mean square system noise, and we use this extensively in connection with the estimators that we consider in the subsequent sections.

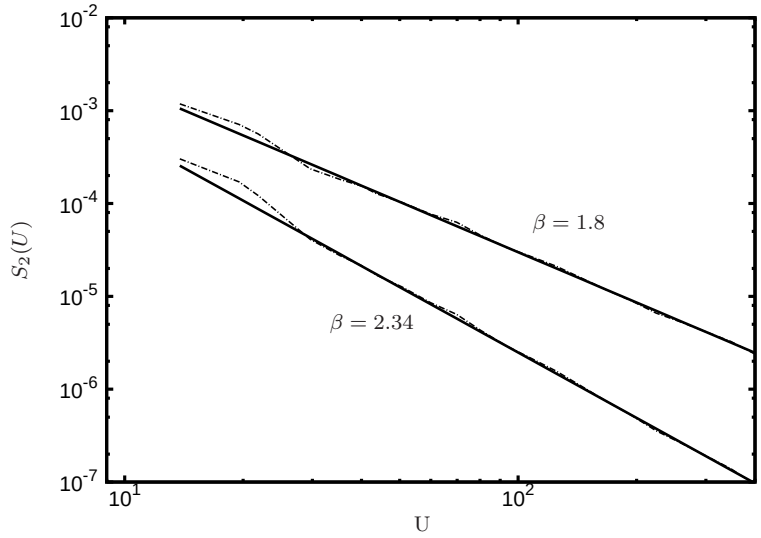

Figure 3. This shows the sky signal contribution to the visibility correlation ($S_2(U)$) for two different power spectra with slopes $\beta = 1.8$ and 2.34 respectively. The dash-dot curve shows the result of the convolution in eq.(9) with $\Delta\mathbf{U} = 0$ whereas the solid curve shows the result of approximating this with eq. (11). We see that the approximation of eq. (11) matches the convolution reasonable well at large baselines $U \geq 4U_0 \sim 45$.

3 SIMULATING THE SKY SIGNAL

We have used simulations of radio-interferometric observations to validate the angular power spectrum estimators that we introduce in subsequent sections of this paper. In this section we first describe the simulations of the sky signal, and then describe how these were used to simulate the expected visibilities. For the sky model, we assume that all point sources with flux above a sufficiently low threshold have been identified and removed from the data so that the 150 MHz radio sky is dominated by the diffuse Galactic Synchrotron radiation.

The slope β of the angular power spectrum of diffuse Galactic synchrotron emission is within the range 1.5 to 3 as found by all the previous measurements at frequencies $0.15 - 94$ GHz (e.g. La Porta et al. 2008; Bernardi et al. 2009). For the purpose of this paper we assume that the fluctuations in the diffuse Galactic Synchrotron radiation are a statistically homogeneous and isotropic Gaussian random field whose statistical properties are completely specified by the angular power spectrum. Further, we assume that the angular power spectrum of brightness temperature fluctuations is well described by a single power law over the entire range of angular scales of our interest. In this work we have adapted the angular power spectrum

$$C_\ell^M = A_{150} \times \left(\frac{1000}{\ell}\right)^\beta, \tag{14}$$

where $A_{150} = 513\,\mathrm{mK}^2$ and $\beta = 2.34$. from Ghosh et al. (2012). This is the input model for all our simulations.

We have considered a $5.8^\circ \times 5.8^\circ$ FoV for the GMRT simulations. This has been represented using a 2048×2048 grid with an angular resolution of ~ 10.2 arcsecond . We have first generated the Fourier components of the brightness temperature fluctuations on the grid using ,

$$\Delta\tilde{T}(\mathbf{U}) = \sqrt{\frac{\Omega\, C_\ell^M}{2}}[x(\mathbf{U}) + iy(\mathbf{U})], \tag{15}$$

where Ω is the total solid angle of the simulation, and $x(\mathbf{U})$ and $y(\mathbf{U})$ are independent Gaussian random variables with zero mean and unit variance. We then use a Fourier transform to generate the brightness temperature fluctuations $\delta T(\vec{\theta})$ or equivalently the specific intensity fluctuations $\delta I(\vec{\theta})$ on the grid. Figure 4 shows one realization of the brightness temperature fluctuations generated using the procedure outlined above. We have generated 20 different independent realizations of the sky by considering different sets of random numbers in eq. (15).

To simulate GMRT observations we consider 8 hr observations targeted on a field located at $+60^\circ$ DEC for which the uv tracks for baselines within $\mid u \mid, \mid v \mid \leq 1,000$ are shown in Figure 5. We assume 16s integration time for each sampled visibility data which gives us $2,17,457$ visibility points. To calculate the visibilities, we have multiplied the simulated $\delta I(\vec{\theta})$ with the primary beam pattern $\mathcal{A}(\vec{\theta})$ (eq. 2) and evaluated the Fourier transform of the product for each sampled baseline $\mathbf{U}$ on the uv track. In addition to the sky signal, each measured visibility will also have a system noise contribution. We have included

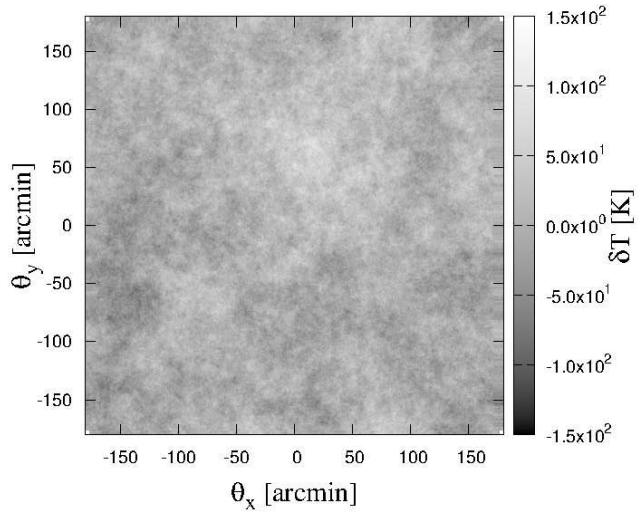

Figure 4. This shows a single realization of the simulated 150 MHz radio sky under the assumption that the bright point sources have been removed so that it is dominated by the diffuse Galactic synchrotron radiation. We have simulated a $5.8^\circ \times 5.8^\circ$ FoV with $\sim 10.2''$ resolution.

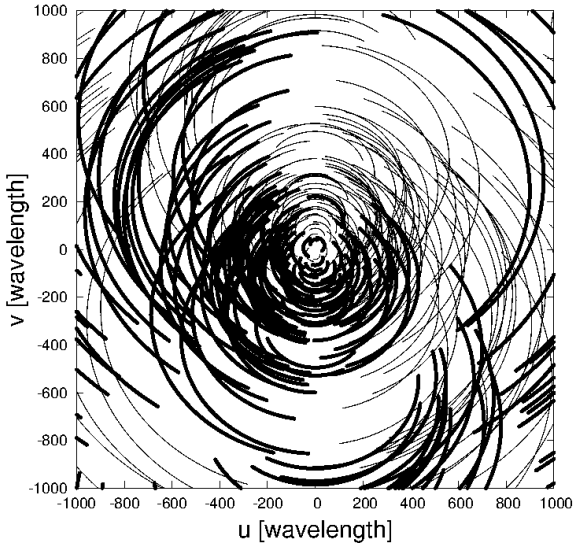

Figure 5. This shows the uv coverage for 8 hr GMRT 150 MHz observations centered on a field at a declination of $\delta = +60^\circ$. Only baselines with $\mid u \mid, \mid v \mid \leq 1,000$ have been shown. Note that u and v are antenna separations measured in units of the observing wavelength, and hence they are dimensionless.

this by adding independent Gaussian random noise contributions to both the real and imaginary parts of each visibility. This noise is predicted to have an rms. of $\sigma_n = 1.03$ Jy for a single polarization at the GMRT[1].

It is clearly visible in Figure 5 that the GMRT has a rather sparse uv coverage. The fact that we have data for only a limited number of the Fourier modes is expected to play an important role. This is particularly important for the cosmic variance which crucially depends on the number of independent Fourier modes. In order to assess the impact of the sparse

[1] http://www.gmrt.ncra.tifr.res.in

uv coverage we have also considered a situation where exactly the same number of visibility measurements $(2,17,457)$ are randomly distributed within the region $\mid u \mid, \mid v \mid \leq 1,000$ on the uv plane.

In the subsequent sections of this paper we have analyzed 20 independent realizations of the sky signal, with visibilities points that correspond to the uv tracks shown in Figure 5. We refer to this ensemble of 20 simulated data sets as "GMRT". We have also considered a random baseline distribution and calculated the visibilities for the same 20 realizations of the sky signal, and we refer to this as "Random". Finally, we have also carried out simulations for LOFAR which has a more uniform uv coverage as compared to the GMRT. These simulations are separately discussed in Section 9.

Finally, we note that the simulated baselines lying in the lower half of the uv plane (e.g. Figure 5.) are all folded to the upper half using the property $\mathcal{V}(\mathbf{U}) = \mathcal{V}^*(-\mathbf{U})$. The simulated baseline distribution that we finally use for analysis is entirely restricted to the upper half of the uv plane.

4 THE BARE ESTIMATOR

The Bare Estimator directly uses the individual visibilities to estimate the angular power spectrum. Each measured visibility corresponds to a Fourier mode of the sky signal, and the visibility squared $\mid \mathcal{V}\mathcal{V}^* \mid$ straight away gives the angular power spectrum. This simple estimator, however, has a severe drawback because the noise contribution $2\sigma_n^2$ is usually much larger than the sky signal $V_0\, e^{-|\Delta \mathbf{U}_{ij}|^2/\sigma_0^2}\, C_\ell$ in eq. (13). Any estimator that includes the correlation of a visibility with itself suffers from a very large positive noise bias. It is, in principle, possible to model the constant noise bias and subtract it out. This however is extremely difficult in practice because small calibration errors (discussed later in Section 7) would introduce fluctuations in the noise bias resulting in residuals that could exceed the sky signal. It is therefore desirable to avoid the noise bias by considering estimators which do not include the contribution from the correlation of a visibility with itself.

The Bare Estimator $\hat{E}_B(a)$ is defined as

$$\hat{E}_B(a) = \frac{\sum_{i,j}\, w_{ij}\, \mathcal{V}_i\, \mathcal{V}_j^*}{\sum_{i,j}\, w_{ij} V_0 e^{-|\Delta \mathbf{U}_{ij}|^2/\sigma_0^2}}\,, \tag{16}$$

where we have assumed that the baselines have been divided into bins such that all the baselines U in the range $U_1 \leq U < U_2$ are in bin 1, those in the range $U_2 \leq U < U_3$ are in bin 2 etc., and $\hat{E}_B(a)$ refers to a particular bin a. The sum i,j is over all pairs of visibilities $\mathcal{V}_i, \mathcal{V}_j$ with baselines $\mathbf{U}_i, \mathbf{U}_j$ in bin a. We have restricted the sum to pairs within $\mid \mathbf{U}_i - \mathbf{U}_j \mid \leq \sigma_0$ as the pairs with larger separations do not contribute much to the estimator. The weight $w_{ij} = (1-\delta_{ij})K_{ij}$ is chosen such that it is zero when we correlate a visibility with itself, thereby avoiding the positive noise bias.

We now show that $\hat{E}_B(a)$ gives an unbiased estimate of the angular power spectrum C_ℓ for bin a. The expectation value of the estimator can be expressed using eq. (13) as

$$\langle \hat{E}_B(a) \rangle = \frac{\sum_{i,j}\, w_{ij}\, V_{2ij}}{\sum_{i,j}\, w_{ij} V_0 e^{-|\Delta \mathbf{U}_{ij}|^2/\sigma_0^2}} = \frac{\sum_{i,j}\, w_{ij}\, e^{-|\Delta \mathbf{U}_{ij}|^2/\sigma_0^2} C_{\ell_i}}{\sum_{i,j}\, w_{ij} e^{-|\Delta \mathbf{U}_{ij}|^2/\sigma_0^2}} \tag{17}$$

which can be written as

$$\langle \hat{E}_B(a) \rangle = \bar{C}_{\bar{\ell}_a} \tag{18}$$

where $\bar{C}_{\bar{\ell}_a}$ is the average angular power spectrum at

$$\bar{\ell}_a = \frac{\sum_{i,j}\, w_{ij}\, e^{-|\Delta \mathbf{U}_{ij}|^2/\sigma_0^2} \ell_i}{\sum_{i,j}\, w_{ij} e^{-|\Delta \mathbf{U}_{ij}|^2/\sigma_0^2}}\,. \tag{19}$$

which is the effective angular multipole for bin a.

We note that it is possible to express eq. (17) using matrix notation as

$$\langle \hat{E}_B(a) \rangle = \frac{Tr(\mathbf{w}\mathbf{V}_2)}{Tr(\mathbf{w}\mathbf{I}_2)} \tag{20}$$

where we have the matrices $\mathbf{w} \equiv w_{ij}$, $\mathbf{V}_2 \equiv V_{2ij}$, $\mathbf{I}_2 = V_0 e^{-|\Delta \mathbf{U}_{ij}|^2/\sigma_0^2}$ and $Tr(\mathbf{A})$ denotes the trace of a matrix $\mathbf{A}$.

We next evaluate $\sigma^2_{\hat{E}_B}(a)$ the variance of $\hat{E}_B(a)$. This gives δC_{ℓ_a} which is an estimate of the error in the angular power spectrum measured from the data. We have

$$[\delta C_{\ell_a}]^2 \equiv \sigma^2_{\hat{E}_B}(a) = \langle \hat{E}_B^2(a) \rangle - \langle \hat{E}_B(a) \rangle^2 \tag{21}$$

which can be simplified to

$$\sigma^2_{\hat{E}_B}(a) = \frac{\sum_{i,j,k,l}\, w_{ij} w_{kl} V_{2il} V_{2kj}}{[Tr(\mathbf{w}\mathbf{I}_2)]^2} = \frac{Tr(\mathbf{w}\mathbf{V}_2\mathbf{w}\mathbf{V}_2)}{[Tr(\mathbf{w}\mathbf{I}_2)]^2} \tag{22}$$

under the assumptions that $\mathbf{w}$ is symmetric and the measured visibilities are Gaussian random variables.

The system noise only appears in the diagonal elements of the visibility correlation matrix $\mathbf{V}_2$, whereas the sky signal

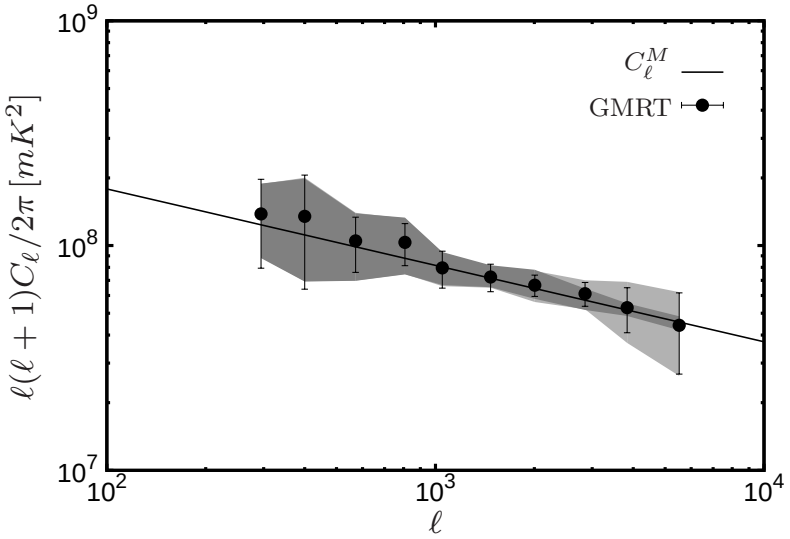

Figure 6. This shows C_ℓ multiplied with $\ell(\ell+1)/2\pi$, plotted as a function of ℓ. The solid line shows the input model (eq. 14) used for the simulations, and the points show the values recovered by the Bare Estimator (eq. 16). The points show the mean and the light shaded region shows the 1σ variation measured from 20 realizations of the GMRT simulations. The dark shaded region shows the cosmic variance which has been calculated by setting the system noise $\sigma_n = 0$ in the simulation, and the error bars show 1σ error bars predicted using eq. (22). The errors are dominated by the cosmic variance at $\ell \leq 2,500$ where the dark and faint shaded regions coincide. We see that the Bare Estimator correctly recovers the input model, and the predicted error bars are consisted with the errors measured from the simulations.

contributes to both the diagonal and the off-diagonal elements. Further, the diagonal elements of the weight matrix $\mathbf{w}$ are all zero. Consequently the trace $Tr(\mathbf{w}\mathbf{V}_2)$ in eq. (18) does not pick up any contribution from the diagonal elements of $\mathbf{V}_2$, and the expectation value of the estimator is not affected by the system noise. The variance $\sigma^2_{E_B}(a)$ however has contributions from both diagonal and off-diagonal elements of $\mathbf{V}_2$. The diagonal elements are dominated by the system noise, whereas the off-diagonal elements contribute to the cosmic variance.

The weights w_{ij} should, in principle, be chosen so as to maximize the signal to noise ratio SNR $= \langle \hat{E}_B(a) \rangle / \sigma_{E_B}(a)$. The optimal weights depend on the baseline distribution and $V_0 C_\ell/\sigma_n^2$, the relative amplitude of the signal to the noise in the individual visibilities. Here we have made the simplifying assumption that all the visibility pairs contribute equally to $\sigma^2_{E_B}(a)$. Each visibility pair is assigned the weight $w_{ij} = (1-\delta_{ij}) e^{-|\Delta \mathbf{U}_{ij}|^2/\sigma_0^2}$ which is proportional to its contribution to $\langle \hat{E}_B(a) \rangle$.

To test the Bare Estimator we have used it to estimate C_ℓ from the simulated GMRT and Random data. For this analysis the visibilities with baselines U in the range $40 \leq U \leq 1,000$ were divided in 20 equally spaced logarithmic bins. Figure 6 shows the mean and the rms. variation of $\ell(\ell+1)C_\ell/2\pi$ measured from the 20 independent realizations of the data. We find that the angular power spectrum estimated from the simulated GMRT data is in good agreement with the model (eq. 14) that was used to simulate the data. We next test the predicted error estimate δC_ℓ given by eq. (22). To do this we have evaluated $\sigma^2_{E_B}(a)$ by explicitly carrying out the sum $\sum_{ijkl}$ where the indices each runs over all the baselines in bin a. For $\mathbf{V}_2$ (eq. 13) we have used the mean C_ℓ estimated from the 20 realizations and the value of σ_n that was used for the system noise in the simulation. We find that δC_ℓ predicted by the analytic error estimate (eq. 22) is in reasonably good agreement with the rms. obtained from the 20 independent realizations of the data. The results for the Random data are very similar to those for GMRT, and we have not shown these separately here.

In conclusion of this section we find that the Bare Estimator (eq. 16) is able to successfully extract the angular power spectrum directly from the measured visibilities. We further show that (eq. 22) provides a reasonably good estimate of the statistical errors for the measured angular power spectrum. The errors depend on the choice of the weights w_{ij}, the baseline distribution, the magnitude of the signal and the system noise. In Figure 6 we see that the error decreases with increasing ℓ until $\ell \sim 2,500$ beyond which the error increases again. We find that this feature does not change significantly between the GMRT and the Random simulations. Based on this we conclude that this behaviour of the error is largely determined by the relative contributions from the signal whose magnitude falls with ℓ and the system noise which has been assumed to be constant across all baselines. The errors at $\ell \leq 2,500$ are cosmic variance dominated, whereas the errors are dominated by the system noise at larger ℓ.

5 THE TAPERED GRIDDED ESTIMATOR

The telescope primary beam is usually not very well quantified at large angles where we have the frequency dependent pattern of nulls and sidelobes (Figure 1). Point sources located near the nulls and the sidelobes are a problem for estimating the angular power spectrum of the diffuse background radiation. Further, point sources located far away from the pointing center, particularly those located near the nulls, introduce ripples along the frequency direction in the multi-frequency angular power spectrum. This poses a severe problem for separating the foregrounds from the cosmological 21-cm signal. As pointed out in Ghosh et al. (2011b), it is possible to avoid these problems by tapering the sky response through a frequency independent window function $\mathcal{W}(\theta)$. In this work we choose a Gaussian $\mathcal{W}(\theta) = e^{-\theta^2/\theta_w^2}$ such that $\theta_w = f\theta_0$ with $f \leq 1$ so that the window function cuts off the sky response well before the first null. This tapering is achieved by convolving the measured visibilities

$$\mathcal{V}_c(\mathbf{U}) = \tilde{w}(\mathbf{U}) \otimes \mathcal{V}(\mathbf{U}) \tag{23}$$

where $\tilde{w}(\mathbf{U}) = \pi\theta_w^2 e^{-\pi^2 U^2 \theta_w^2}$ is the Fourier transform of $\mathcal{W}(\theta)$. The convolved visibilities $\mathcal{V}_c(\mathbf{U})$ are the Fourier transform of the product $\mathcal{W}(\theta)\,\mathcal{A}(\theta)\,\delta I(\vec{\theta})$ whose sky response can be well controlled through the window function $\mathcal{W}(\theta)$.

Current radio interferometers are expected to produce considerably large volumes of visibility data in observations spanning many frequency channels and large observing times. Given the potentially large computational requirement, it is useful to compress the visibility data by gridding it. We choose a rectangular grid in the uv plane and consider the convolved visibilities

$$\mathcal{V}_{cg} = \sum_i \tilde{w}(\mathbf{U}_g - \mathbf{U}_i)\,\mathcal{V}_i \tag{24}$$

where $\mathbf{U}_g$ refers to the different grid points and $\mathcal{V}_i$ refers to the measured visibilities. We now focus our attention on $\mathcal{S}_{cg} = \sum_i \tilde{w}(\mathbf{U}_g - \mathbf{U}_i)\,\mathcal{S}_i$ which is the sky signal contribution to $\mathcal{V}_{cg}$. This can be written as

$$\mathcal{S}_{cg} = \int d^2U\, \tilde{w}(\mathbf{U}_g - \mathbf{U}) B(\mathbf{U}) \mathcal{S}(\mathbf{U}) \tag{25}$$

where $B(\mathbf{U}) = \sum_i \delta_D^2(\mathbf{U} - \mathbf{U}_i)$ is the baseline sampling function of the measured visibilities and $\delta_D^2(\mathbf{U})$ is the 2D Dirac delta function. The integral in eq. (25) is dominated by the contribution from within a disk of radius $\sim (\pi\theta_w)^{-1}$ centered around $\mathbf{U}_g$. Assuming that the sampling function $B(\mathbf{U})$ is nearly uniform within this disk we can replace $B(\mathbf{U})$ in eq. (25) by its average value

$$\bar{B}(\mathbf{U}_g) = \left[\frac{\int d^2U\, \tilde{w}(\mathbf{U}_g - \mathbf{U}) B(\mathbf{U})}{\int d^2U\, \tilde{w}(\mathbf{U}_g - \mathbf{U})}\right] \tag{26}$$

evaluated at the grid point $\mathbf{U}_g$. We then have the approximate equation

$$\mathcal{S}_{cg} = \bar{B}(\mathbf{U}_g) \int d^2U\, \tilde{w}(\mathbf{U}_g - \mathbf{U}) \mathcal{S}(\mathbf{U})\,. \tag{27}$$

Considering eq. (26) for $\bar{B}(\mathbf{U}_g)$, the denominator has value $\mathcal{W}(0) = 1$ whereby $\bar{B}(\mathbf{U}_g) = \sum_i \tilde{w}(\mathbf{U}_g - \mathbf{U}_i)$ and we have

$$\mathcal{S}_{cg} = \left[\sum_i \tilde{w}(\mathbf{U}_g - \mathbf{U}_i)\right] \int d^2U\, \tilde{w}(\mathbf{U}_g - \mathbf{U}) \mathcal{S}(\mathbf{U})\,. \tag{28}$$

We note that eq. (28) holds only if we have an uniform and sufficiently dense baseline distribution in the vicinity of the grid point $\mathbf{U}_g$. This breaks down if we have a patchy and sparse baseline distribution, and it is then necessary to use

$$\mathcal{S}_{cg} = \sum_i \tilde{w}(\mathbf{U}_g - \mathbf{U}_i) \mathcal{S}(\mathbf{U}_i)\,. \tag{29}$$

In such a situation it is necessary to take the exact patchy uv distribution into account, and it is difficult to make generic analytic predictions. Here we have assumed an uniform baseline distribution, and we have used eq. (28) extensively in the subsequent calculations.

The integral in eq. (28) is the Fourier transform of the product $\mathcal{W}(\theta)\,\mathcal{A}(\theta)\,\delta I(\vec{\theta}) \equiv \mathcal{A}_{\mathcal{W}}(\theta)\,\delta I(\vec{\theta})$. We may think of $\mathcal{A}_{\mathcal{W}}(\theta)$ as a modified primary beam pattern which has a new $\theta_{\rm FWHM}$ which is a factor $f/\sqrt{1+f^2}$ smaller than $\theta_{\rm FWHM}$ given in Table 1 and whose sidelobes are strongly suppressed. We can approximate the modified primary beam pattern as a Gaussian $\mathcal{A}_{\mathcal{W}}(\theta) = e^{-\theta^2/\theta_1^2}$ with $\theta_1 = f(1+f^2)^{-1/2}\theta_0$. Using this, we can generalize eq. (13) to calculate the correlation of the gridded visibilities $V_{c2gg'} = \langle \mathcal{V}_{cg} \mathcal{V}_{cg'}^* \rangle$. The crucial point is that we have to replace V_0 and σ_0 in eq. (13) with $V_1 = \frac{\pi\theta_1^2}{2}\left(\frac{\partial B}{\partial T}\right)^2$ and $\sigma_1 = f^{-1}\sqrt{1+f^2}\sigma_0$ in order to account for the modified primary beam pattern $\mathcal{A}_{\mathcal{W}}(\theta)$. We then have

$$V_{c2gg'} = K_{1g} K_{1g'}^* V_1 e^{-|\Delta\mathbf{U}_{gg'}|^2/\sigma_1^2} C_{\ell_g} + 2\sigma_n^2 K_{2gg'} \tag{30}$$

where $\ell_g = 2\pi U_g$, $K_{1g} = \sum_i \tilde{w}(\mathbf{U}_g - \mathbf{U}_i)$, $K_{2gg'} = \sum_i \tilde{w}(\mathbf{U}_g - \mathbf{U}_i)\tilde{w}^*(\mathbf{U}_{g'} - \mathbf{U}_i)$ and $\Delta\mathbf{U}_{gg'} = \mathbf{U}_g - \mathbf{U}_{g'}$.

We now define the estimator $\hat{E}_g$ for the angular power spectrum at a single grid point g as

$$\hat{E}_g = \frac{(\mathcal{V}_{cg}\mathcal{V}_{cg}^* - \sum_i |\, \tilde{w}(\mathbf{U}_g - \mathbf{U}_i)\,|^2\, |\,\mathcal{V}_i\,|^2)}{(|\,K_{1g}\,|^2\, V_1 - K_{2gg} V_0)}\,. \tag{31}$$

Using eq. (30) and eq. (13) respectively to evaluate the expectation values

$$\langle \mathcal{V}_{cg}\mathcal{V}_{cg}^{*}\rangle = \mid K_{1g} \mid^{2} V_1 C_{\ell_g} + 2\sigma_n^2 K_{2gg} \tag{32}$$

and

$$\sum_i \mid \tilde{w}(\mathbf{U}_g - \mathbf{U}_i) \mid^2 \langle \mid \mathcal{V}_i \mid^2 \rangle = V_0 \sum_i \mid \tilde{w}(\mathbf{U}_g - \mathbf{U}_i) \mid^2 C_{\ell_i} + 2\sigma_n^2 K_{2gg} \tag{33}$$

we see that the system noise contributions to these two terms are exactly equal and it exactly cancels out in $\langle \hat{E}_g \rangle$. Further, assuming that $\sum_i \mid \tilde{w}(\mathbf{U}_g - \mathbf{U}_i) \mid^2 C_{\ell_i} \approx C_{\ell_g} K_{2gg}$ we have

$$\langle \hat{E}_g \rangle = C_{\ell_g} \, . \tag{34}$$

We see that $\hat{E}_g$ defined in eq. (31) gives an unbiased estimate of the angular power spectrum C_ℓ avoiding the positive noise bias caused by the system noise.

The terms K_{1g} and K_{2gg} in eq. (31) are both proportional to N_g the number of visibilities that contribute to the grid point g. For large N_g it is reasonable to assume that $\mid K_{1g} \mid^2 \gg K_{2gg}$ and we thereby simplify eq. (31) to obtain

$$\hat{E}_g = \frac{(\mathcal{V}_{cg}\mathcal{V}_{cg}^{*} - \sum_i \mid \tilde{w}(\mathbf{U}_g - \mathbf{U}_i) \mid^2 \mid \mathcal{V}_i \mid^2)}{\mid K_{1g} \mid^2 V_1} \tag{35}$$

for the estimator.

We use this to define the binned Tapered Gridded Estimator

$$\hat{E}_G(a) = \frac{\sum_g w_g \hat{E}_g}{\sum_g w_g} \, . \tag{36}$$

where w_g refers to the weight assigned to the contribution from any particular grid point. This has an expectation value

$$\langle \hat{E}_G(a) \rangle = \frac{\sum_g w_g C_{\ell_g}}{\sum_g w_g} \tag{37}$$

which can be written as

$$\langle \hat{E}_G(a) \rangle = \bar{C}_{\bar{\ell}_a} \tag{38}$$

where $\bar{C}_{\bar{\ell}_a}$ is the average angular power spectrum at

$$\bar{\ell}_a = \frac{\sum_g w_g \ell_g}{\sum_g w_g} \tag{39}$$

which is the effective angular multipole for bin a.

We next calculate the variance of $\hat{E}_G(a)$ defined as

$$[\delta C_{\ell_a}]^2 \equiv \sigma^2_{E_G}(a) = \langle \hat{E}_G^2(a) \rangle - \langle \hat{E}_G(a) \rangle^2 \, . \tag{40}$$

Explicitly using eq. (35) yields a rather unwieldy expression which is not very useful for making analytic predictions for the variance. The first term in the numerator of eq. (35) which is of order N_g^2 makes a much larger contribution to the variance than the second term $\sum_i \mid \tilde{w}(\mathbf{U}_g - \mathbf{U}_i) \mid^2 \mid \mathcal{V}_i \mid^2$ which is of order N_g. In our analysis we make the simplifying assumption that we can drop the second term which yields

$$\sigma^2_{E_G}(a) = \frac{\sum_{gg'} w_g w_g^{'} \mid K_{1g}^{-1} K_{1g'}^{*-1} V_{c2gg'} \mid^2}{V_1^2 [\sum_g w_g]^2} \, . \tag{41}$$

We further approximate $K_{2gg'} = e^{-|\Delta \mathbf{U}_{gg'}|^2/\sigma_1^2} K_{2gg}$ which allows us to write the variance as

$$\sigma^2_{E_G}(a) = \frac{\sum_{gg'} w_g w_g^{'} e^{-2|\Delta \mathbf{U}_{gg'}|^2/\sigma_1^2} \mid C_{\ell_g} + \frac{2K_{2gg'}\sigma_n^2}{K_{1g}K_{1g'}^{*}V_1} \mid^2}{[\sum_g w_g]^2} \tag{42}$$

using eq. (30).

We have applied the Tapered Gridded Estimator to the simulated GMRT and Random data. The 20 realizations were used to calculate the mean and the variance of the estimated C_ℓ. We have considered the values $f = 1.0, 0.8, 0.65$ and 0.4 for the tapering window, and have also tried two different weight schemes $w_g = 1$ and $w_g = K_{1g}^2$ respectively. The former assigns equal weight to every grid point that has same data, this is expected to minimize the cosmic variance. The latter scheme assigns a larger weight to grid points which have a denser visibility sampling relative to the grid points with sparser sampling. This is expected to minimize the system noise contribution. The grid spacing ΔU in the uv plane is chosen based on two considerations. A very small value of ΔU results in a very large number of grid points which do not contain independent signal contributions. This also unnecessarily increases the computation time. In contrast, a large value of ΔU implies that the signal in many visibilities is very poorly represented in the gridded data, resulting in a loss of signal. We have chosen a grid spacing $\Delta u = \sqrt{\ln 2}/(2\pi\theta_w)$ which corresponds to one fourth of the FWHM of $\tilde{w}(\mathbf{U})$ as an optimum value. For any fixed grid

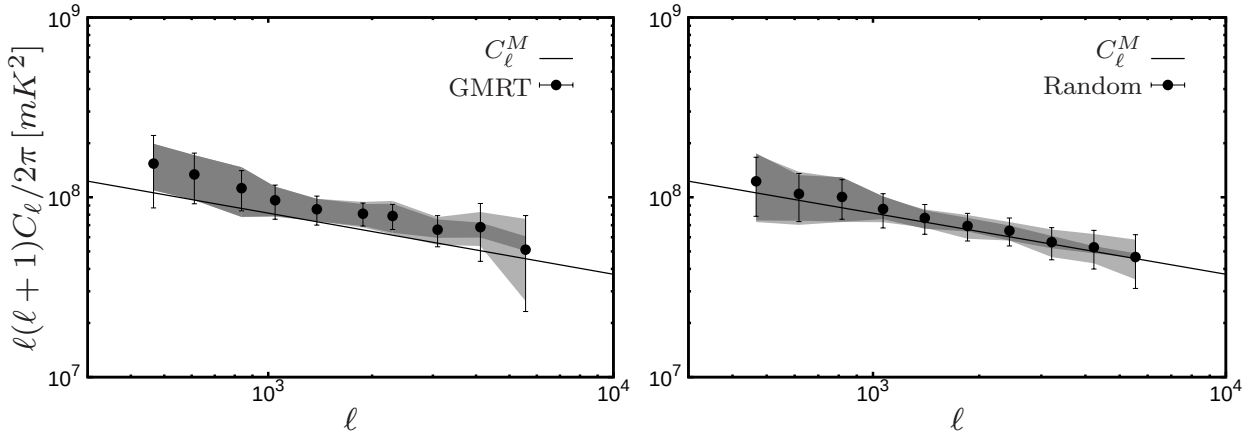

Figure 7. Same as Figure 6, but for the Tapered Gridded Estimator.

position $\mathbf{U}_g$, we have restricted the contribution to baselines $\mathbf{U}_i$ within $\mid \mathbf{U}_g - \mathbf{U}_i \mid \leq 6\Delta U$. The weight function $\tilde{w}(\mathbf{U}_g - \mathbf{U}_i)$ falls considerably and we do not expect a significant contribution from the visibilities beyond this baseline separation. The tapering also modifies the smallest baseline where the approximation of eq. (11) is valid, and the grid points $\mathbf{U}_g$ in the range $U_{min} = \sqrt{1+f^2}f^{-1}40$ to $1,000$ were binned into 10 equally spaced logarithmic bins for this analysis.

Figure 7 shows the results for $f = 0.8$ and $w_g = \mid K_{1g} \mid^2$. We see that for both GMRT and Random the estimated C_ℓ are roughly within the 1σ region of the input model angular power spectrum C_ℓ^M. For GMRT, however, the estimated C_ℓ values all appear to be somewhat in excess of C_ℓ^M indicating that we have an overestimate of the angular power spectrum relative to C_ℓ^M. In comparison, the C_ℓ values are in better agreement with C_ℓ^M for the Random simulation. For both GMRT and Random the error estimates predicted by eq. (42) are in good agreement with the rms. fluctuation estimated from the 20 realizations. We note that the rms. fluctuation of C_ℓ is more for GMRT in comparison to Random.

The Tapered Gridded Estimator is expected to give an unbiased estimate of C_ℓ provided we have a uniform and sufficiently dense baseline distribution. We test this using the Random simulations which have a uniform baseline distribution. In such a situation we expect the deviation $C_\ell - C_\ell^M$ to arise purely from statistical fluctuations. The deviation is expected to have values around $\sigma/\sqrt{N_r}$ and converge to 0 as N_r, the number of realizations, is increased. For this purpose we have studied (Figure 8) how the fractional deviation $(C_\ell - C_\ell^M)/C_\ell^M$ varies if we increase the number of realizations from $N_r = 10$ to 100. We find that it is more convenient to use 20 equally spaced logarithmic bins in ℓ to highlight the convergence of the fractional deviation with increasing N_r. Note that we have used 10 bins (as mentioned earlier) everywhere except in (Figure 8). For the Random simulation (right panel), we find that as the number of realizations is increased the convergence of the fractional deviation to 0 is clearly visible for $\ell \geq 1.2 \times 10^3$ ($U \geq 200$). Further, the fractional deviation is also found to be consistent with $\sigma/(\sqrt{20}\, C_\ell^M)$ and $\sigma/(10\, C_\ell^M)$ expected for $N_r = 20$ and 100 respectively. At smaller baselines, however, the behaviour is not so clear. The approximation eq. (11) for the convolution and the approximation for the primary beam pattern each introduce around $2-5\%$ errors in the estimated C_ℓ at small baselines. Further, for a uniform baseline distribution the bins at the smallest ℓ values contain fewer baselines and also fewer grid points, and are susceptible to larger fluctuations. The discrete uv sampling due to the finite number of baselines is also expected to introduce some errors at all values of ℓ. To test this effect, we have considered a situation where $N_r = 100$ and the total number of baselines is increase to $869,828$ which is a factor of 4 larger compared to the other simulations. We find that for $\ell \geq 3 \times 10^3$ the fractional deviation falls from $\sim 5\%$ to $\sim 2\%$ when the baseline density is increased, this difference is not seen at smaller baselines. In summary, the tests clearly show that for a uniform baseline distribution the estimator is unbiased for $\ell \geq 1.2 \times 10^3$. In contrast, for the GMRT (left panel) the fractional deviation does not converge to 0 as N_r is increased. We see that C_ℓ is overestimated at all values of ℓ. As mentioned earlier, the GMRT has a patchy uv coverage for which eq.(27), which assumes a uniform baseline distribution, breaks down. The overestimate is a consequence of GMRT's patchy uv coverage, and is not inherent to the Tapered Gridded Estimator. The rms. fluctuations also are larger for GMRT in comparison to the Random simulations (Figure 7). This too is a consequence of GMRT's patchy uv coverage.

We now study how the estimator behaves for different values of f. Figure 9 and Figure 10 respectively show the relative deviation $(C_\ell - C_\ell^M)/C_\ell^M$ and the relative error σ/C_ℓ^M for different values of f with $w_g = \mid K_{1g} \mid^2$. Here, C_ℓ and σ refer to the mean and rms. estimated from the 20 realizations. We find that the deviations are roughly within the 1σ errors for all the cases that we have considered. For GMRT, the deviation increases with decreasing f. This effect is only visible at low ℓ for Random. The error σ, increases with f for both GMRT and Random. In all cases, the error is found to decrease until $\ell \sim 2000$ and then increase subsequently. As mentioned earlier for the Bare Estimator, we interpret this as a transition from cosmic variance to system noise dominated errors as ℓ is increased. The sky coverage of the modified primary beam $\mathcal{A}_{\mathcal{W}}(\theta)$

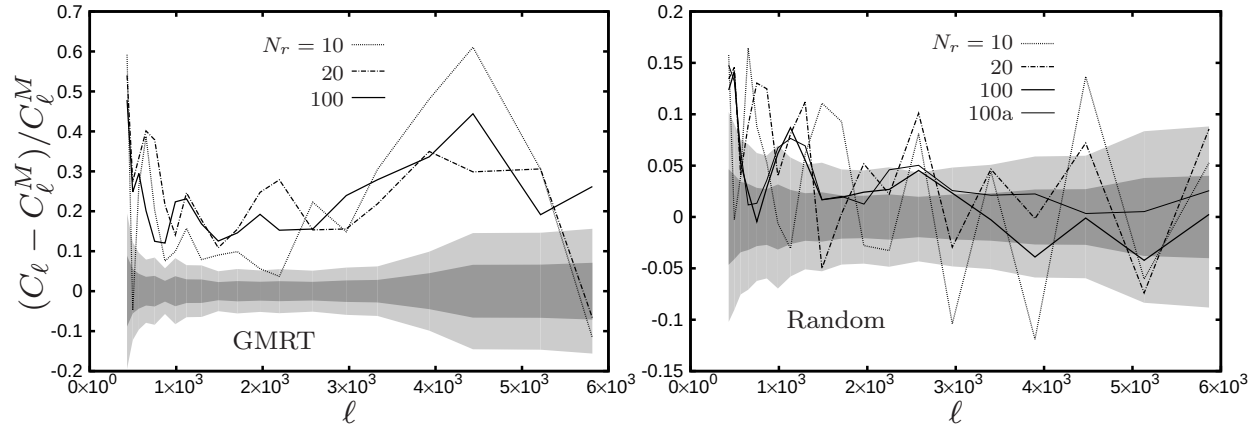

Figure 8. The different curves show the fractional deviation $(C_\ell - C_\ell^M)/C_\ell^M$ for the different numbers of realizations (N_r) shown in the figure. The curve 100a corresponds to $N_r = 100$ with 869, 828 baselines, which is 4 times the number of baselines in the other simulations. The two shaded region show $\sigma/(\sqrt{N_r}\, C_\ell^M)$ for $N_r = 20$ and 100 respectively. We have used $f = 0.8$ and $w_g =\mid K_{1g} \mid^2$, with 20 equally spaced logarithmic bins in ℓ.

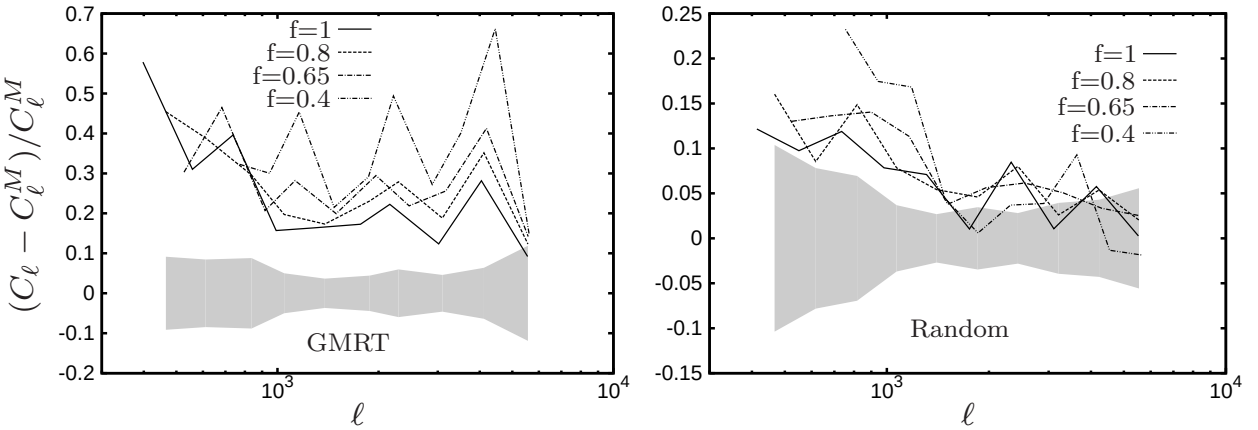

Figure 9. This shows how the fractional deviation varies with f for $w_g =\mid K_{1g} \mid^2$. The results are averaged over 20 realizations of the sky signal. For comparison, the shaded region shows $\sigma/(\sqrt{20}\, C_\ell^M)$ which is the expected statistical fluctuation for $f = 0.8$.

falls with a decrease in f. This explains the bahaviour of the cosmic variance contribution which increases as f is reduced. We further see that the system noise contribution also increases as f is reduced. This can be attributed to the term $V_1 = \frac{\pi\theta_1^2}{2}$ which appears in eq. (42). This effectively increases the system noise contribution relative to C_ℓ as f is reduced.

We have studied the relative performance of the two weight scheme mentioned earlier. Figure 11 shows the relative deviation and the relative error for both $w_g = 1$ and $w_g =\mid K_{1g} \mid^2$ for $f = 0.8$. As expected, the first scheme performs better in the cosmic variance dominated regime. The difference between the two weight scheme, however, is not very large in this regime. The second weight scheme performs significantly better in the system noise dominated region. In this region the errors are nearly doubled if we use $w_g = 1$ instead of $w_g =\mid K_{1g} \mid^2$.

In summary, we have introduced a Gridded Estimator for the angular power spectrum where it is possible to avoid the positive noise bias which arises due to the contribution from the correlation of a visibility with itself. Further, the estimator allows the possibility to taper the sky response and thereby implement sidelobe suppression. We have used simulated visibility data to validate the estimator. We find that the estimator provides an unbiased estimate of C_ℓ for $\ell \geq 1.2 \times 10^3$ if we have a sufficiently dense, uniform baseline distribution. We also find that eq. (42) provides a good analytic estimate of the errors in the measured C_ℓ. The estimator is found to be sensitive to the telescope's uv coverage, and we have somewhat of an overestimate for the GMRT which has a patchy uv coverage. This deviation, however, is roughly within the 1σ error bars and is not expected to be a serious issue. It is possible to carry out simulations with the actual observational uv coverage and use these to compensate for the overestimate. The new telescopes like LOFAR (discussed later) have a denser and more uniform uv coverage, and we do not expect this issue to be of concern there. The 1σ errors, we find, increase as the tapering is increased. The choice of f, however, is decided by issues related to point source removal not considered here. We find that the weight scheme $w_g =\mid K_{1g} \mid^2$ performs better than $w_g = 1$, and we use the former for the subsequent analysis.

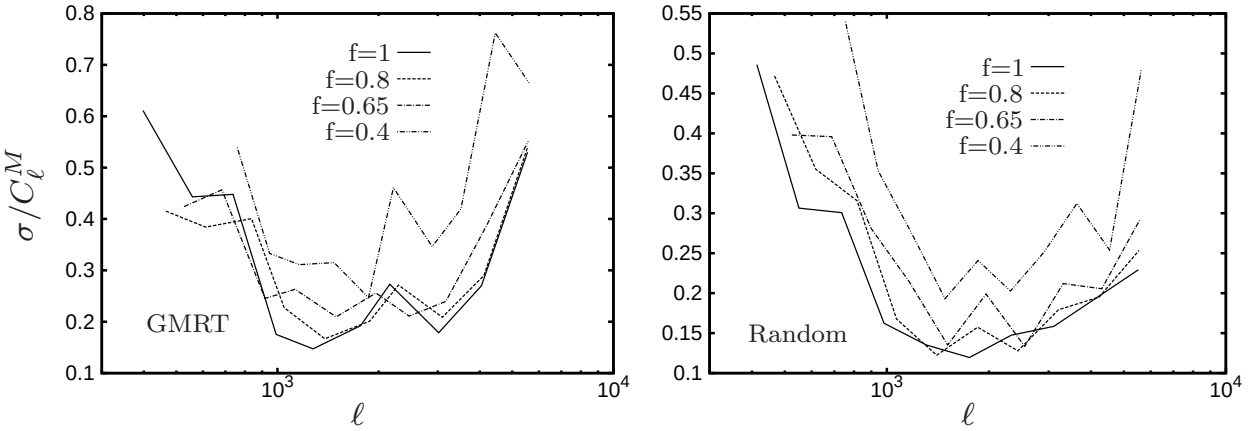

Figure 10. This figure shows the relative error (σ/C_ℓ^M) estimated from 20 realization of the simulation. Here, we have used $w_g =\mid K_{1g} \mid^2$ and the different f values shown in this figure.

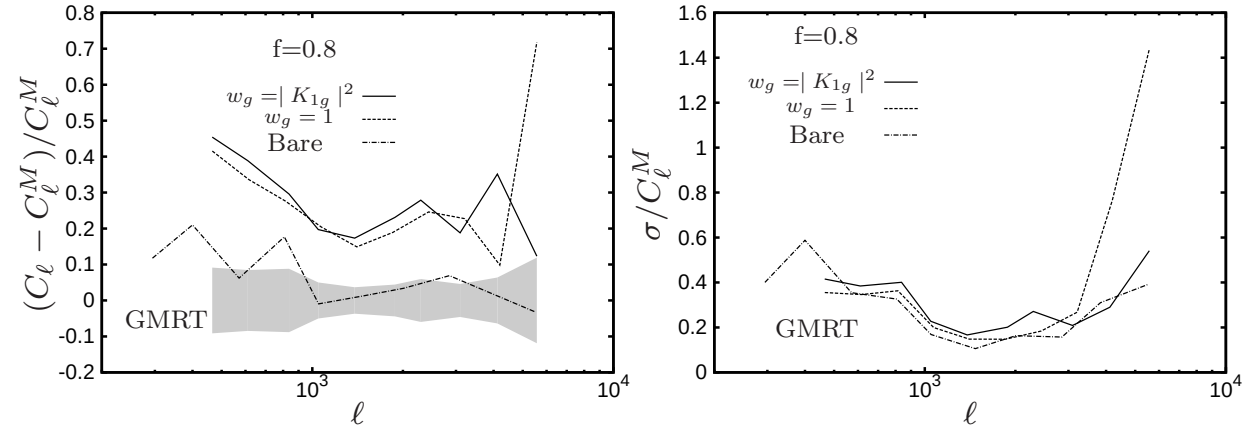

Figure 11. The left (right) panel shows the fractional deviation (error) for the two weight schemes $w_g = 1$ and $\mid K_{1g} \mid^2$ respectively, both with $f = 0.8$. The results for the Bare estimator have also been shown for comparison. The results are based on 20 realizations of the sky signal. For comparison, the shaded region in the left panel shows $\sigma/(\sqrt{20}\, C_\ell^M)$ which is the expected statistical fluctuation for $w_g =\mid K_{1g} \mid^2$.

6 A COMPARISON OF THE TWO ESTIMATORS

Comparing the Bare Estimator with the Tapered Gridded Estimator we see (left panel of Figure 11) that the former is more successful in recovering the input sky model. The statistical errors also (right panel of Figure 11) , we find, are somewhat smaller for the Bare Estimator. The Bare Estimator deals directly with the measured visibilities, and in a sense we expect it to outperform any other estimator which deals with gridded visibilities. What then is the motivation to consider a Gridded Estimator which is not able to recover the input model with as much accuracy as the Bare Estimator? The Bare Estimator deals directly with the visibilities and the computational time for the pairwise correlation in eq. (16) scales proportional to N^2, where N is the total number of visibilities in the data. Further, the error calculation in eq. (22) is expected to scale as N^4. In contrast, the computation time is expected to scale as N for Tapered Gridded Estimator. This N dependence arises in the process of gridding the visibilities, the correlation eq. (35) and the error estimate eq. (42) are both independent of N.

Figure 12 show the computation time for the two estimators as the number of visibilities varied. We see that the computation time shows the expected N dependence for large values of $N(> 1000)$. The Bare Estimator takes less computation time when N is small ($N \leq 10^4$). However, the computation time for the Bare Estimator and its error estimate are larger than that for the Tapered Gridded Estimator for $N \geq 10^5$. The Bare Estimator is extremely computation extensive for a large N and it is preferable to use the Gridded Estimator when $N \geq 10^5$. Based on this we focus on the Tapered Gridded Estimator for most of the subsequent discussion.

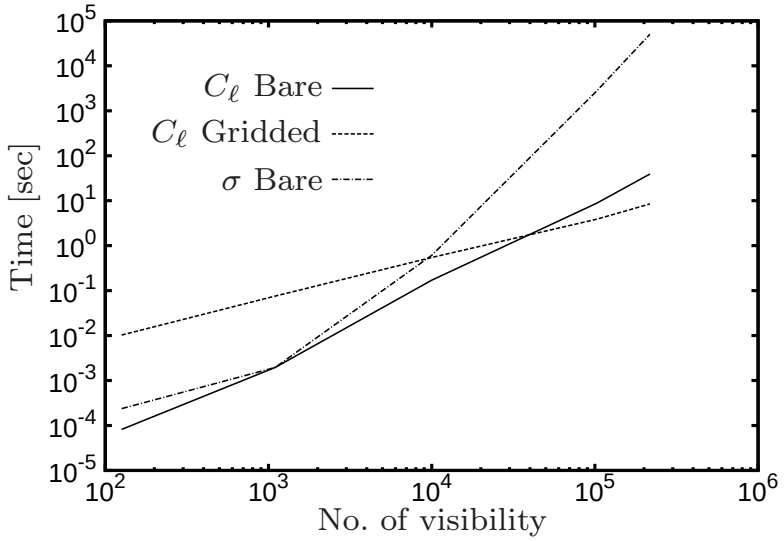

Figure 12. This shows how the computation time varies with the number of visibility data for the two different estimators. The computation time for analytically predicting the error (eq. 22) for the Bare Estimator is also shown.

7 GAIN ERRORS

The measured visibilities have undetermined time varying gains which arise due to the atmosphere, receiver system, etc. The calibration procedure attempts to determine these gains and correct for them, but this generally leaves unknown residual gain errors in the data. Datta et al. (2009, 2010) have studied the impact of the residual gain errors on bright source subtraction and place a tolerance limit for detecting the reionization 21 cm signal. Recently, Shaw et al. (2014b) have discussed how amplifier gains affect on the detection of the 21 cm signal from post-reionization and reionization era respectively. Here we study the effect of gain errors on the estimators that we have defined earlier. For this work we assume antenna dependent gain errors whereby the calibrated visibilities can be written as

$$\mathcal{V}(\mathbf{U}_{ab}) = g_a g_b^* [\mathcal{S}(\mathbf{U}_{ab}) + \mathcal{N}(\mathbf{U}_{ab})] \tag{43}$$

where a, b refer to the two antennas corresponding to the baseline $\mathbf{U}_{ab}$, and $g_a = (1+\alpha_a)e^{i\phi_a}$ and $g_b = (1+\alpha_b)e^{i\phi_b}$ are the respective antenna gains. Here the α_as and the ϕ_as are respectively the amplitude and the phase errors of the individual antenna gains. We have assumed that both α_a and ϕ_a are Gaussian random variables of zero mean and variance σ_α^2 and σ_ϕ^2 respectively. The errors are assumed to be independent in different antennas and at different time instants .

The two visibility correlation can be written as,

$$\langle \mathcal{V}(\mathbf{U}_{ab}) \mathcal{V}^*(\mathbf{U}_{cd}) \rangle = \langle g_a g_b^* g_c^* g_d \rangle [S_2(\mathbf{U}_{ab}, \mathbf{U}_{cd}) + N_2(\mathbf{U}_{ab}, \mathbf{U}_{cd})] \tag{44}$$

where the product of the gains is to be averaged over different realizations of the gain errors α and ϕ. We now have three different possibilities which we discussed below.

Case I: The two visibilities $\mathcal{V}(\mathbf{U}_{ab})$ and $\mathcal{V}(\mathbf{U}_{cd})$ are at two different time instants or they have no antenna in common. In this situation we have

$$\langle g_a g_b^* g_c^* g_d \rangle = e^{-2\sigma_\phi^2}. \tag{45}$$

Case II: The two visibilities $\mathcal{V}(\mathbf{U}_{ab})$ and $\mathcal{V}(\mathbf{U}_{cd})$ are at the same time instant and have only one antenna in common. In this situation we have

$$\langle g_a g_b^* g_c^* g_d \rangle = (1+\sigma_\alpha^2) e^{-\sigma_\phi^2}. \tag{46}$$

Case III: Both $\mathcal{V}(\mathbf{U}_{ab})$ and $\mathcal{V}(\mathbf{U}_{cd})$ referred the same measured visibility. In this situation we have

$$\langle g_a g_b^* g_c^* g_d \rangle = (1+\sigma_\alpha^2)^2. \tag{47}$$

The signal contribution to both the estimators defined earlier is dominated by Case I, whereas the noise is dominated by Case III. Based on this it is possible to generalize eq. (13) to obtain the approximate relation

$$V_{2ij} = e^{-2\sigma_\phi^2} V_0 \, e^{-|\Delta \mathbf{U}_{ij}|^2/\sigma_0^2} \, C_{\ell_i} + (1+\sigma_\alpha^2)^2 \delta_{ij} 2\sigma_n^2 \tag{48}$$

which takes into account the effect of gain errors. It is also possible to generalize eq. (30) for the gridded visibilities in a

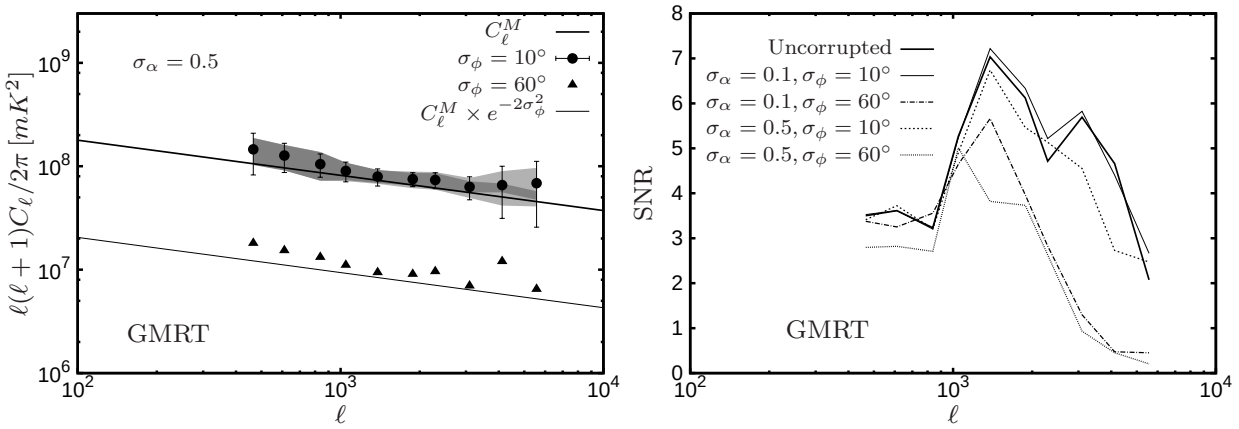

Figure 13. The left panel shows the same as Figure 6 for the Tapered Gridded Estimator using corrupted visibilities with the σ_α and σ_ϕ values shown in the figure. We have also shown $e^{-2\sigma_\phi^2} \times C_\ell^M$ with $\sigma_\phi = 60°$ for comparison. The right panel shows the SNR for different values of σ_α and σ_ϕ.

similar fashion. Using these to calculate the effect of gain errors on the estimators defined earlier, we have

$$\langle \hat{E}(a) \rangle = e^{-2\sigma_\phi^2} \bar{C}_{\bar{\ell}_a} \, . \tag{49}$$

for both the Bare and the Tapered Gridded Estimators. We see that both the estimators are unaffected by the error in the gain amplitude, however the phase errors cause the expectation value of the estimator to decrease by a factor $e^{-2\sigma_\phi^2}$. It is quite straightforward to generalize eq. (22) and eq. (41) to incorporate the effect of the gain errors in the variance of the Bare and the Tapered Gridded Estimators respectively. The main effect is that the signal contribution is suppressed by a factor $e^{-2\sigma_\phi^2}$ whereas the system noise contribution is jacked up by a factor $(1+\sigma_\alpha^2)^2$ (eq. 48). We consequently expect the SNR to remain unchanged in the cosmic variance dominated regime at low ℓ, whereas we expect the SNR to fall in the system noise dominated regime (large ℓ). Further, we also expect the transition from the cosmic variance to the system noise dominated regime to shift to smaller ℓ values if the gain errors increase.

We have carried out simulations to test the effect of gain errors on the angular power spectrum estimators. For this we have generated 20 different realizations of the random gain errors and used these to corrupt the simulated visibilities described in Section 3. The simulations were carried out for different values of σ_α and σ_ϕ. We have applied both the Bare and the Tapered Gridded Estimators on the corrupted visibilities. Both the estimators show very similar behaviour under gain errors, and we show the results for only the Tapered Gridded Estimator.

We have considered two values $\sigma_\alpha = 0.1$ and 0.5 which respectively correspond to 10% and 50% errors in the gain amplitude. The left panel of Figure 13 shows the results for $\sigma_\alpha = 0.5$. We see that the expectation value of the estimator is unaffected by the errors in the gain amplitude. For the phase errors, we have considered the values $\sigma_\phi = 10°$ and $60°$ for which $e^{-2\sigma_\phi^2}$ have values 0.94 and 0.11 respectively. The left panel of Figure 13 shows that eq. (49) provides a good description for the effect of the gain errors on the angular power spectrum estimator. We see the net result of the phase errors is that the estimated angular power spectrum is reduced by a factor $e^{-2\sigma_\phi^2}$ relative to the input model.

The right panel of Figure 13 shows the SNR for different values of σ_α and σ_ϕ. The rms. fluctuation σ_{E_G} of the estimator is expected to depend exponentially as $e^{-2\sigma_\phi^2}$ on the phase errors and have a $(1+\sigma_\alpha^2)^2$ dependence on the amplitude errors (eq. 48). We find that the simulated SNR are more sensitive to the phase errors in comparison to the amplitude errors. The SNR is nearly invariant to gain errors in the cosmic variance dominated regime (low ℓ) where σ_{E_G} is reduced by the same factor $e^{-2\sigma_\phi^2}$ as the expectation value of the estimator. However, the transition from the cosmic variance dominated to the system noise dominated regime (approximately the peak of the SNR curves) shifts to smaller ℓ if the gain errors are increased. The amplitude errors, we see, reduces the SNR at large ℓ where the error is dominated by the system noise.

8 THE W-TERM

The entire analysis, until now, has been based on the assumption that the visibility contribution $\mathcal{S}(\mathbf{U})$ from the sky signal is the Fourier transform of the product of $\mathcal{A}(\vec{\theta})$ and $\delta I(\vec{\theta})$. This is only an approximate relation which is valid only if the filed of view is sufficiently small. The actual relation is

$$\mathcal{S}(u,v,w) = \int dl dm \frac{\delta I(l,m)\mathcal{A}(l,m)}{\sqrt{1-l^2-m^2}} e^{-2\pi i[ul+vm+w(\sqrt{1-l^2-m^2}-1)]} \, , \tag{50}$$

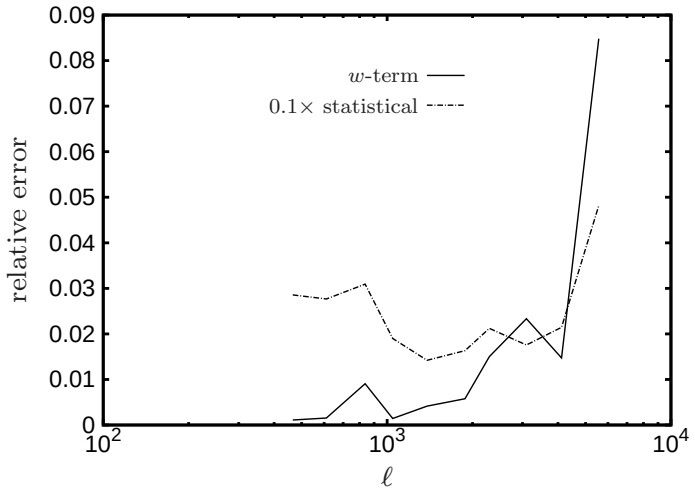

Figure 14. This shows the relative change in the estimated angular power spectrum using Tapered Gridded Estimator due to the w-term. For comparison we have also shown $0.1 \times \delta C_\ell / C_\ell$ which corresponds to 10% of the relative statistical error in C_ℓ.

where the w-term, which we have ignored until now, is the baseline component along the line of sight to the phase center and l, m are the direction cosines corresponding to any point on the sky. In a situation where the primary beam pattern falls of within a small angle from the phase center, it is adequate to treat the region of sky under observation as a 2D plane and use $(l, m) = (\theta_x, \theta_y)$. For example, the GMRT has a FWHM of $186^{'}$ for which $\sqrt{1 - l^2 - m^2} \approx 0.997$. The term $\sqrt{1 - l^2 - m^2}$ which appears in the denominator of eq. (50) incorporates the curvature of the sky. We see that this makes an insignificant contribution at the small angles of our interest, and hence may be ignored. The term $w(\sqrt{1 - l^2 - m^2} - 1)$ which appears in the phase in eq. (50) has a value $\sim 10^{-3} \times w$ for the angle mentioned earlier, and this is not necessarily small. The value of w depends on the telescope configuration and the observing direction, and may be quite large ($> 10^3$). It is therefore necessary to assess the impact of the w-term on the angular power spectrum estimators defined earlier.

We have simulated GMRT visibilities using eq. (50) keeping the w-term. The 20 realizations of the sky signal and the baseline tracks are the same as described in section 3, and we have used the flat sky approximation (*i.e.* we have dropped $\sqrt{1 - l^2 - m^2}$ from the denominator). We have applied both the Bare and the Tapered Gridded Estimator to this simulated visibility data. We show results for only the Tapered Gridded Estimator, the results are very similar for the Bare Estimator and we have not shown these separately. Figure 14 shows the relative change in the estimated angular power spectrum if we include the w-term. We find that the change due to the w-term is less than 3% for all values of ℓ barring the largest ℓ value where there is a 9% change. The w-term has a larger effect at the large baselines which also correspond to a larger value of w. We find that the change caused by the w-term is less than 10% of the statistical fluctuations for most values of ℓ. In summary, for angular power spectrum estimation it is adequate to ignore the w-term at the angular scales of our interest for the GMRT.

9 LOFAR

LOFAR, the Low Frequency Array, is an innovative new radio telescope which operates at the lowest radio frequencies ($10 - 240$ MHz) (var Haarlem et al. 2013). It consists of an interferometric array of dipole antenna stations distributed throughout the Netherlands and Europe. The individual stations perform the same basic functions as the dishes of a traditional interferometric radio telescope. Hence, the station beam which is analogous to the primary beam ultimately determines the FoV for a given observation. In the High Band Antennas (HBAs, $110-240$ MHz), groups of dipole pairs are combined into HBA tiles and the station beam is formed from the combined signal from the tiles. The HBA tiles are sensitive to two orthogonal linear polarizations. Close to the phase centre, the LOFAR station beam can be well modelled with a circular Gaussian and the FWHM of the Gaussian varies approximately from 3.0° to 5.0° in the frequency range $115 - 185$ MHz with $\theta_{\rm FWHM} = 3.8^\circ$ at 150 MHz.

In this section we consider the possibility of using LOFAR to estimate the angular power spectrum of the 150 MHz sky signal after point source subtraction. The LOFAR has a wider field of view compared to the GMRT and we have simulated a $\sim 8^\circ \times 8^\circ$ region of the sky with an angular resolution of $14^{''} \times 14^{''}$. Here again we have generated 20 independent realizations of the sky signal. The simulations were carried out in exactly the same way as described in Section 3 using the LOFAR parameters given in Table 1. We have generated the LOFAR baseline distribution for the 62 antennas in the central core region for 8 hrs of observing time. Visibilities were generated with a time interval of 40s and we obtain a total of $669,809$

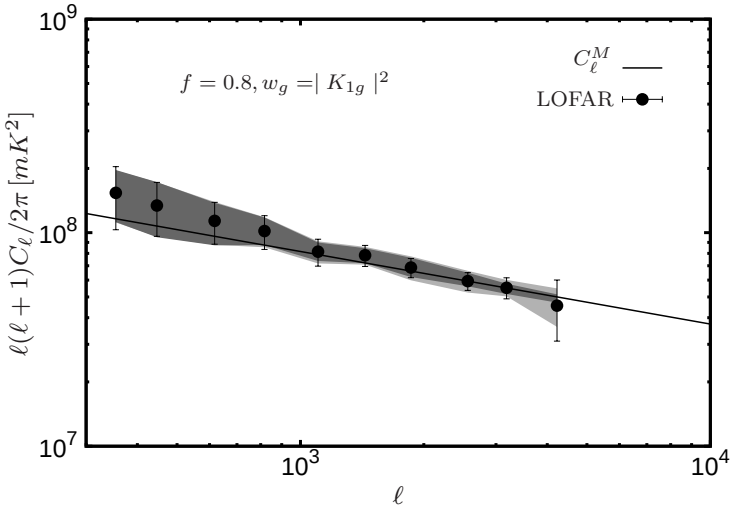

Figure 15. Same as Figure 6 for the Tapered Gridded Estimator and the simulated LOFAR data.

visibilities in the baseline range $30 \leq \mathbf{U} \leq 800$. We have included the w-term for calculating the LOFAR visibilities. The LOFAR has a denser uv coverage compared to the GMRT, and the simulated baseline range is nearly uniformly covered. We have used $\sigma_n = 2.2$Jy (var Haarlem et al. 2013) for the system noise in the simulations. Given the large volume of data, we have only used the Tapered Gridded Estimator with $f = 0.8$ and $w_g = K_{1g}^2$.

Figure 15 shows the angular power spectrum estimated from our simulations. We see that the estimated C_ℓ values are all within the 1σ region of the input model angular power spectrum C_ℓ^M. The estimated C_ℓ values, however, are somewhat in excess of C_ℓ^M at small ℓ ($< 1,000$). The fractional deviation $(C_\ell - C_\ell^M)/C_\ell^M$ is around $\sim 30\%$ at the smallest ℓ bin, and it is $\sim 15\%$ at $\ell \sim 800$. The excess is not seen at larger ℓ where the estimated values are in excellent agreement with C_ℓ^M. We also see that the error estimates predicted by eq. (42) are in good agreement with the rms. fluctuation estimated from the 20 realizations. The transition from cosmic variance dominated errors to system noise dominated errors occurs at $\ell \sim 2,000$ similar to the GMRT. The LOFAR has considerably more baselines compared to the GMRT, and the errors in the estimated angular power spectrum are smaller for LOFAR in comparison to GMRT.

As mentioned earlier in the context of the GMRT, the excess in the estimated C_ℓ may be a consequence of patchy uv coverage at small baselines ($U < 160$). The average baseline density in the region $U < 160$ is several times larger than the average within $U < 800$, however this does not guaranty that the former is less patchier than the latter. Further, it is not possible to say anything definite from a visual inspection of the baseline distribution. The convolution with the primary beam pattern and the window function introduces a $\sim 8\%$ deviation between C_ℓ and C_ℓ^M at $U < 160$. The exact cause of the excess at small ℓ is at present not fully understood.

10 DISCUSSION AND CONCLUSIONS

In this paper we have introduced two estimators for quantifying the angular power spectrum of the sky brightness temperature. Both of these estimators use the visibilities measured in radio interferometric observations. The Bare Estimator works directly with the measured visibilities, and uses pairwise visibility correlations to estimate the angular power spectrum. The Tapered Gridded Estimator uses the visibility data after gridding on a rectangular grid in the uv plane. Here it is possible to taper the sky response so as to suppress the sidelobes and reduce the filed of view. Earlier work (Ghosh et al. 2011b) shows tapering to be an important ingredient in foreground removal for detecting the cosmological 21-cm signal. We have investigated the properties of the estimators, and present analytic formulae for the expectation value (eqs. 18 and 38) and the variance (eqs. 22 and 42). The expectation value of both the estimators is free from the positive system noise bias which arises due to the correlation of a visibility with itself. The system noise affects only the variance.

We have carried out simulations to validate the estimators. The simulated sky signal assumes that the point sources have been removed and the residuals are dominated by the diffuse Galactic synchrotron radiation which is modelled as a homogeneous and isotropic Gaussian random field with a power law angular power spectrum. We consider GMRT observations for most of the analysis. We find that the Bare Estimator is able to recover the input model to a good level of precision. The computation time is found to scale as N^2 with the number of visibility data. Further, the scaling is N^4 for the variance.

We find that the Tapered Gridded Estimator is able to recover the input model C_ℓ^M to a high level of precision provided the baselines have a uniform uv coverage. For the GMRT which has a patchy uv coverage, the C_ℓ estimated from the Tapered

Gridded Estimator is largely within the 1σ errors from the input model C_ℓ^M. There is, however, indication that the angular power spectrum is overestimated to some extent. Comparing the results to a situation with a uniform random baseline distribution, we conclude that the overestimate is a consequence of GMRT's patchy uv coverage and is not inherent to the Tapered Gridded Estimator which is unbiased in the ideal situation of uniform uv coverage. It is possible to use simulations to quantify this overestimate and correct for this in a real observation. We do not anticipate this overestimate to be a very major obstacle for the Tapered Gridded Estimator. The computation time for this estimator and its variance both scale as N. Long observations spanning many frequency channels will produce large volumes of visibility data. The Bare Estimator is computationally very expensive for large N, and a Gridded Estimator is the only feasible alternative. Consequently, we have focused on the Tapered Gridded Estimator for much of the analysis in the later part of this paper.

Residual gain errors corrupt the measured visibilities, and this is a potential difficulty for estimating the angular power spectrum. We have analyzed the effect of gain errors on the two estimators introduced in this paper. Our analysis, validated by simulations, shows that the expectation value of the estimators is unaffected by amplitude errors. The phase errors cause a decrement by the factor $e^{-2\sigma_\phi^2}$ in the expectation value. The statistical errors in the estimated C_ℓ are affected by both the amplitude and the phase errors, however this is more sensitive to the phase errors relative to the amplitude errors. We have also investigated the effect of the w-term. We find that the w-term does not cause a very big change in the estimated C_ℓ at the scales of our interest here. Our analysis here shows that the residual phase errors can lead to the angular power spectrum being underestimated by a factor $e^{-2\sigma_\phi^2}$ which has a value ~ 0.1 for $\sigma_\phi = 60^\circ$. It is therefore imperative to independently quantify the magnitude of the residual phase errors for a correct estimate of the angular power spectrum.

In addition to GMRT, we have also applied the estimators to simulated LOFAR data. We find that the C_ℓ estimated using the Tapered Gridded Estimator is within the 1σ errors of the input model. There is, however, indication that there is some overestimation $(15-30\%)$ at low ℓ $(< 1,000)$. The exact cause of this excess at small ℓ is at present not fully understood.

The two estimators considered here both avoid the positive noise bias which arises due to the system noise contribution in the visibilities. This is achieved by not including the contribution from the correlation of a visibility with itself. As an alternative one could consider an estimator which straight away squared the measured or the gridded visibilities. In this situation it is necessary to separately identify the noise bias contribution and subtract it out. The noise bias contribution is expected to be independent of frequency and ℓ. It is, in principle, possible to identify a frequency and ℓ independent component and subtract it out. However, our analysis in this paper shows that the errors in the amplitude of the calibrated gains affect the noise bias. Frequency and baseline dependent gain errors would manifest themselves as the frequency and ℓ dependence of the noise bias. This is a major obstacle which is bypassed by our estimators.

The multi-frequency angular power spectrum (MAPS, Datta, Roy Choudhury & Bharadwaj 2007) jointly quantifies the angular and frequency dependence of the fluctuations in the sky signal. This can be estimated directly from the measured visibilities (e.g. Ali, Bharadwaj & Chengalur 2008), and it can be used to detect the cosmological 21-cm signal (Ghosh et al. 2011b). In future work we plan to generalize the analysis of this paper to the multi-frequency angular power spectrum and address various issues, including point source removal, which are relevant for detecting the cosmological 21-cm signal.

11 ACKNOWLEDGEMENTS

SC would like to acknowledge UGC, India for providing financial support. SB would like to thank Ayesha Begum, Jayaram N. Chengalur, Prasun Dutta and Jasjeet S. Bagla for useful discussions. AG acknowledge the financial support from the European Research Council under ERC-Starting Grant FIRSTLIGHT - 258942. SSA would like to acknowledge C.T.S, I.I.T. Kharagpur for the use of its facilities and the support by DST, India, under Project No. SR/FTP/PS-088/2010. SSA would also like to thank the authorities of the IUCAA, Pune, India for providing the Visiting Associateship programme.

References

Ali S. S., Bharadwaj S.,& Chengalur J. N., 2008, MNRAS, 385, 2166A
Ali, S. S., & Bharadwaj, S. 2014, Journal of Astrophysics and Astronomy, 35,157
Bernardi, G., de Bruyn, A. G., Brentjens, M. A., et al. 2009, A & A, 500, 965
Bernardi, G., de Bruyn, A. G., Harker, G., et al. 2010, A & A, 522, A67
Begum, A., Chengalur, J. N., & Bhardwaj, S. 2006, MNRAS, 372, L33
Bennett C.L., Hill R.S., Hinshaw. G. et al., 2003, ApJS, 148, 97
Bowman J. D., Morales M. F., & Hewitt J. N. 2009, Ap.J, 695, 183
Bharadwaj S., & Sethi S. 2001, JApA, 22, 293
Bharadwaj S. ,& Pandey S. K., 2003, JApA, 24, 23
Bharadwaj S. , & Ali S. S. 2005, MNRAS, 356, 1519
Chapman, E., Abdalla, F. B., Harker, G., et al. 2012, MNRAS, 423, 2518

Chapman, E., Abdalla, F. B., Bobin, J., et al. 2013, MNRAS, 429, 165
Christiansen, W. N. & Hogbom, J. A., 1969, Radio telescopes, second edition, Cambridge Univ. Press
Cho, J., Lazarian, A., & Timbie, P. T. 2012, Ap.J, 749, 164
Datta K. K., Roy Choudhury, T.,& Bharadwaj. S, 2007, MNRAS, 378, 119
Datta A., Bhatnagar S., & Carilli C. L. 2009, Ap.J, 703, 1851
Datta, A., Bowman, J. D., & Carilli, C. L. 2010, Ap.J, 724, 526
Dillon, J. S., Liu, A., Williams, C. L., et al. 2014, PRD, 89, 023002
Dutta P., Begum A., Bharadwaj S., & Chengalur J. N. 2009, MNRAS, 398, 887
Ghosh, A., Bharadwaj, S., Ali, S. S., & Chengalur, J. N. 2011a, MNRAS, 411, 2426
Ghosh, A., Bharadwaj, S., Ali, S. S., & Chengalur, J. N. 2011b, MNRAS, 418, 2584
Ghosh, A., et al. 2012, MNRAS, 426, 3295
Giardino, G., Banday, A. J., Fosalba, P., et al. 2001, A & A, 371, 708
Giardino, G., Banday, A. J., Górski, K. M., et al. 2002, A & A, 387, 82
Hobson M.P., Lasenby A.N., Jones M., 1995, MNRAS, 275, 863
Hobson M.P., Maisinger K., 2002, MNRAS, 334, 569
Iacobelli, M., Haverkorn, M., Orrú, E., et al. 2013, A & A, 558, A72
Jacobs, D. C., Bowman, J., & Aguirre, J. E. 2013, Ap.J, 769,5
Jelic V., et al., 2010, MNRAS, 409, 1647
La Porta, L., Burigana, C., Reich, W., & Reich, P. 2008, A & A, 479, 641
Lazarian, A., & Pogosyan, D. 2012, Ap.J, 747, 5
Liu, A., & Tegmark, M. 2012, MNRAS, 419, 3491
Liu, A., Parsons, A. R., & Trott, C. M. 2014a, PRD, 90, 023018
Liu, A., Parsons, A. R., & Trott, C. M. 2014b, PRD, 90, 023019
Mao, X.-C. 2012, Ap.J, 744, 29
Myers S.T., et al., 2003, ApJ, 591, 575
Mellema, G., et al. 2013, Experimental Astronomy, 36, 235
Morales, M. F., & Wyithe, J. S. B. 2010, ARAA, 48, 127
Parsons, A. R., Liu, A., Aguirre, J. E., et al. 2014, Ap.J, 788, 106
Paul, S., Sethi, S. K., Subrahmanyan, R., et al. 2014, arXiv:1407.4620
Paciga G. et al., 2011, MNRAS, 413, 1174
Paciga, G., Albert, J. G., Bandura, K., et al. 2013, MNRAS, 433, 639
Petrovic, N., & Oh, S. P. 2011, MNRAS, 413, 2103
Pober, J. C., Parsons, A. R., Aguirre, J. E., et al. 2013, Ap.JL, 768, L36
Shaw, J. R., Sigurdson, K., Pen, U.-L., Stebbins, A., & Sitwell, M. 2014a, Ap.J, 781, 57
Shaw, J. R., Sigurdson, K., Sitwell, M., Stebbins, A., & Pen, U.-L. 2014b, arXiv:1401.2095
Thyagarajan, N., Udaya Shankar, N., Subrahmanyan, R., et al. 2013, Ap.J, 776, 6
Trott, C. M., Wayth, R. B., Macquart, J.-P. R., & Tingay, S. J. 2011, Ap.J, 731, 81
Trott, C. M., Wayth, R. B., & Tingay, S. J. 2012, Ap.J, 757, 101
van Haarlem, M. P., Wise, M. W., Gunst, A. W., et al. 2013, A & A, 556, A2
Vedantham, H., Udaya Shankar, N., & Subrahmanyan, R. 2012, Ap.J, 745, 176
Waelkens, A. H., Schekochihin, A. A., & Enßlin, T. A. 2009, MNRAS, 398, 1970
White M., Carlstrom J.E., Dragovan M., Holzapfel S.W.L., 1999, ApJ, 514, 12